Air-Sea fluxes of CO2 in the Indian Ocean between 1985 and 2018: A synthesis based on Observation-based surface CO2 , hindcast and atmospheric inversion models

V.V.S.S. Sarma, B. Sridevi, Nicolas Metzl, P. K. Patra, Z. Lachkar, Kunal Chakraborty, C. Goyet, Marina Lévy, M. Mehari, N. Chandra

Air-Sea fluxes of CO_2 in the Indian Ocean between 1985 and 2018: A synthesis based on Observation-based surface CO_2, hindcast and atmospheric inversion models.

VVSS Sarma[1], B. Sridevi[1], N. Metzl[2], P. K. Patra[3], Z. Lachkar[4], Kunal Chakraborty[5], C. Goyet[6,7], M. Levy[2], M. Mehari[4], N. Chandra[3]

[1]CSIR-National Institute of Oceanography, Regional Centre, 176 Lawsons Bay Colony, Visakhapatnam, India

[2]LOCEAN/IPSL laboratory, Sorbonne Université, CNRS/IRD/MNHN, Paris, France

3Japan Agency for Marine-Earth Science and Technology, Kanagawa, Japan

[4]Arabian Center for Climate and Environmental Sciences, New York University Abu Dhabi, Abu Dhabi, United Arab Emirates

[5]Indian National Centre for Ocean Information Services, Ministry of Earth Sciences, Hyderabad, India

[6]Espace-Dev, UPVD, Perpignan France

[7]Espace-Dev, Univ. Montpellier, UPVD, IRD, Montpellier, France

Abstract

The Indian Ocean significantly influences the global carbon cycle but it is one of the undersampled regions in the global ocean with reference to surface ocean pCO_2. As a part of the Regional Carbon Cycle Assessment and Processes-2 (RECCAP2) project, several approaches, such as interpolated observational climatology, hindcast model, observation-based surface CO_2 (empirical models), and atmospheric inversion models have been employed for estimating net sea-to-air CO_2 fluxes between 1985 and 2018. The seasonal, spatial and long-term variability in sea-to-air fluxes of CO_2 were compared with observational climatology. The mean value of CO_2 in the Indian Ocean (north of 37.5^{o}S) using all models is estimated to be -0.19±0.1 PgC yr^{-1} and it is consistent with the observational climatology (-0.07±0.14 PgC yr^{-1}). The Indian Ocean north of 18^{o}S is found to

be the mean annual source (0.04±0.05 PgC yr^{-1}) whereas a net sink (-0.23±0.11 PgC yr^{-1}) in the south of 18°S. All models captured observed spatial patterns but underestimated the net source of CO_2 in the Oman/Somalia upwelling, the Equatorial Indian Ocean (EIO) and the Bay of Bengal (BoB) whereas CO_2 sink is overestimated in the South Indian Ocean (SIO). Overall, all models captured the seasonality in pCO_2 levels and CO_2 fluxes but overestimated the amplitude of their variability. All models suggested the strengthening of the sink over the period between 1985 and 2018 by 0.02 PgC yr^{-1} $decade^{-1}$. A significant increase in the collection of surface ocean pCO_2 and atmospheric CO_2 measurements improves the model simulations in the Indian Ocean.

Keywords: Surface pCO_2; CO_2 fluxes; Hindcast models; atmospheric inversions; Indian Ocean

1. Introduction

The atmospheric carbon dioxide (CO_2) levels are ever increasing since the Industrial Revolution due to several anthropogenic activities such as fossil fuel burning and land-use changes. The enhanced anthropogenic activities led to the acceleration of the rate of CO_2 accumulation in the atmosphere from ~1.7±0.1 PgC yr^{-1} in the 1960s to 5.3±0.1 PgC yr^{-1} in 2021 (Friedlingstein et al., 2022). About half of the total anthropogenic emission remains in the atmosphere, and the remaining half is stored in the ocean and land (Canadell et al. 2021). According to the Global Carbon Project assessment of 2022, the ocean has taken up about 28% (2.9±0.4 PgC yr^{-1}) of the total anthropogenic CO_2 emissions during 2021 (Friedlingstein et al., 2022). It is also well established that the ocean carbon sink increased since the 60s with inter-annual variability (IAV) not fully captured by ocean models.

The Indian Ocean is a small basin compared to the other two major basins of the Pacific and Atlantic and has a unique geography as it is closed in the north at a low latitude. More than 30% of the global population is dwelling along the Indian Ocean coast where rapid industrialization is taking place. As a result, the highest levels of aerosol optical depth (AOD) are observed over the northern Indian Ocean with the highest rate of increase over the globe (Zhang and Reid, 2010; Yadav et al., 2021). The northeastern Indian Ocean (Bay of Bengal; BoB) receives a significant amount of freshwater from major rivers, such as the Ganges, Brahmaputra, and Irrawaddy-Salween systems. The northern Indian Ocean experiences strong seasonality due to a change in direction of monsoonal wind resulting in a reversal in direction of surface currents (Schott and McCreary, 2001), which strongly modulates the biogeochemical cycling of carbon and nitrogen. The northern Indian Ocean is one of the most

productive regions in the globe and contributes up to 20% of global ocean primary productivity (Behrenfield and Falkowski, 1997).

Despite the importance of the Indian Ocean in the global carbon cycle, this region is poorly studied with reference to the biogeochemical cycling of carbon compared to the other two major basins. The seasonal cycle of pCO_2 and carbon fluxes was studied only in the Arabian Sea (George et al., 1994; Goyet et al., 1998; Sarma et al., 1998; 2003; 2013, De Verneil et al., 2022; Chakraborty et al., 2021), the BoB (Sarma et al., 2012; 2015; 2020; 2021; Chakraborty et al., 2021) and the south-western Indian ocean (Metzl et al., 1998) whereas the long-term variability was only recently studied in the southwestern Indian Ocean region (Metzl et al., 2022) as the other regions in the Indian Ocean was either sampled once or twice during last few decades (Takahashi et al., 2009; Sarma et al., 2013). The studies carried out in the aegis of the Joint Global Flux Study (JGOFS) and the Bay of Bengal Process Studies (BoBPS) suggested that the seasonal amplitude of pCO_2 goes beyond 200 μatm in the Arabian Sea (George et al., 1994; Goyet et al., 1998; Sarma et al., 1998; 2003) and BoB (Kumar et al., 1996; Sarma et al., 2012; 2015; 2019). The large amplitude of variability in pCO_2 is driven by variabilities in physical transport, such as upwelling, and convective mixing, in the Arabian Sea, whereas freshwater input by rivers and atmospheric pollutants deposition in the BoB (Sarma et al., 2000; 2012). River discharge displays significant inter-annual variability (Papa et al., 2012). Sarma et al. (2012) found that peninsular rivers bring acidic and high pCO_2 waters to the coast whereas glacial rivers, such as Ganges and Brahmaputra, bring relatively basic and low pCO_2 waters to the BoB. Therefore, the source of river water determines the direction of the flux of CO_2 at the air-sea interface. Kumar et al. (1996) suggested that the BoB is a sink for atmospheric CO_2 in the 1990s whereas Sarma et al. (2015; 2021) found that it is a mild source of the atmosphere due to the deposition of

atmospheric pollutants. More recently Sridevi and Sarma (2021) indicated that salinity in the surface waters of the BoB is decreasing over the past two decades due to an increase in the warming of Himalayan glaciers (Goes et al., 2020). Since the pH of the Ganges and Brahmaputra River waters are relatively basic (Sarma et al., 2012), an increase in pH and a decrease in pCO_2 was noticed in the past two decades in the central and eastern BoB (Sridevi and Sarma, 2021).

Unlike the other two major basins, upwelling is weak in the equatorial Indian Ocean due to the prevalence of westerly winds along the equatorial Indian Ocean (Schott et al., 2009). A flat thermocline is observed in the equatorial Indian Ocean in the east-west direction (Murtugudde and Bualacchi, 1999; Xie et al., 2002). The southern tropical and subtropical region is influenced by the inflow of Pacific waters from the Indonesian Through Flow (ITF) (Schott and McCreary, 2001). A major subduction zone occurs in the South Indian Ocean between 15 and 50^{o}S due to positive wind stress curl (Schott et al., 2009). The subducted water masses are advected to the northern Indian Ocean (Miyama et al., 2003; Schott et al., 2002), carrying nutrients and anthropogenic CO_2 (Sabine et al., 1999). A perennial sink of atmospheric CO_2 was reported in the south Indian Ocean (SIO; Metzl et al., 1991; Poisson et al., 1993; Metzl et al., 1995; 1998; 2022; Metzl, 2009).

The Indian Ocean experiences strong zonal variability driven by the Indian Ocean Dipole/Zonal Mode (IOD/IODZM) in addition to El Nino-Southern Oscillation (ENSO) and the Southern Annular Mode (SAM) (Saji et al., 1999; Murthugude et al., 2000; Thompson and Solomon, 2002). These climate modes of variability modulate several physical and biogeochemical processes resulting in significant modifications in the CO_2 flux (Sarma 2006; Valsala et al., 2020). The influence of SAM was suggested in the SIO for the period 1991-

2007 with large spatial variability in CO_2 growth rate with lower rates in the north of 40°S than south of 40°S during austral winter but higher and uniform rates during austral summer (Metzl, 2009).

Gruber et al. (2009) identified a significant mismatch between top-down and bottom-up inversion in the tropical Indian Ocean and attributed it to a lack of atmospheric CO_2 data. Sarma et al. (2013) compared CO_2 fluxes from the Indian Ocean between 1990 and 2009 using a suite of models (both ocean biogeochemistry and atmospheric inversions) under the aegis of the RECCAP1 project. For the band 30°N-44°S, the median annual sea-air CO_2 flux from models was -0.37±0.06 PgC yr^{-1} and it was consistent with -0.24±0.12 PgC yr^{-1} using observations. They further noticed that although all models captured the spatial patterns, CO_2 outgassing was underestimated in the upwelling region and overestimated sink in the BoB, whereas CO_2 uptake was underestimated in the subtropical convergence zone.

Recent use of regional models to study the dynamics of regional ecosystems and biogeochemical cycles in the Indian Ocean revealed an improved representation of key processes relative to global coarse resolution models. For instance, the representation of oxygen minimum zones (OMZ) in the northern Indian Ocean indicates large discrepancies with observations in both CMIP5 and CMIP6 global models, but shows a much-improved agreement with data in regional model simulations, both in terms of their structure, size and intensity (Bopp et al., 2013, Cocco et al., 2013, Kwiatkowski et al., 2020, Al Azhar et al., 2017, Lachkar et al., 2016, 2018, 2021). This was linked to the importance of eddy fluxes - typically inaccurately parameterized in global coarse-resolution models but resolved in finer-resolution regional models – in shaping OMZs (e.g., Lachkar et al., 2016, Bettencourt et al., 2015, Brandt et al., 2015, Chakraborty et al., 2019). Furthermore, accurately representing the

structure and intensity of these low-O_2 bodies in regional models is critical to represent their recent and future changes under ongoing climate change (Lachkar et al., 2021). Mesoscale eddies were also shown to have a significant impact on the carbon cycle in the northern Indian Ocean (Sarma et al., 2016; 2019; 2021). Additionally, significant improvements in parameterizations of river discharge, monsoon mixing and associated biological response in the high-resolution regional models lead to a better representation of the upper ocean cycle in the regional models (Chakraborty et al., 2018; 2021; Ghosh et al., 2022; Valsala et al., 2021). Therefore, eddy-resolving regional models may lead to an improved representation of the carbon cycle in the region. This work aims to evaluate the net air-sea CO_2 fluxes by different global and regional models and quantify how these simulated net CO_2 fluxes in the Indian Ocean are comparable with observational climatology and identify potential reasons for deviations, if any, in the Indian Ocean.

2. Methods

2.1. Study region

Based on the RECCAP2 regional definitions, the entire Indian Ocean, north of 37.5^{o}S, was considered as one region. Due to the complexity of the regional physical processes in the Indian Ocean, we define here the following five regions for analysis: i) the entire Indian Ocean (30^{o}N-37.5^{o}S), ii) the Arabian Sea (0-30^{o}N; 38-78^{o}E), iii) the Bay of Bengal (BoB; 0-30^{o}N; 78-110^{o}E), iv) Equatorial Indian Ocean (EIO; 0-18^{o}S) and v) South Indian Ocean (SIO; 18^{o}S-37.5^{o}S) (Figure 1a).

2.2 Data sets

To describe the regional CO_2 fluxes for the Indian Ocean, RECCAP2 global CO_2 flux products were used that include observations (climatology referenced to the year 2000; Takahashi et al., 2009), Global hindcast (GHM), regional hindcast (RHM) models, observation-based (empirical) surface pCO_2 models and atmospheric inversion models.

2.2.1. Observational climatology

The Indian Ocean is one of the least sampled basins in the world ocean for surface pCO_2 measurements with reference to space and time (Figure 1b; Bakker et al., 2016). The major addition of data was done during 1990-1999 whereas in the next decade (2000-2009) some data were added in the SIO and one transect in the BoB and good coverage of the Bay was done in 2010-2019 (Bakker et al., 2020; Supplementary Figure S1). Within the Indian Ocean, the seasonal and inter-annual pCO_2 data are available in the western basin (the Arabian Sea and the southwestern Indian Ocean). In contrast, only 2 to 3 times were sampled in the eastern basin (Supplementary Figure S1). In addition to this, time-series pCO_2 (water and air) data are available in the central BoB, as a part of the RAMA (Moored array for African-Asian-Australian Monsoon Analysis and Prediction) buoy program (BOBOA, Sutton et al, 2019), from 2013 onwards (Figure 1). Nevertheless, understanding seasonality in pCO_2 is a challenge in the Indian Ocean due to the weak spatial and seasonal data coverage. Takahashi et al. (2009) (Figure 1c) compiled the available pCO_2 data in the Indian Ocean and gridded it to 4^o x 5^o using two-dimensional advection-diffusion equations to interpolate with reference to space and time. The major challenge here is that the observations (henceforth called climatology) are not absolutely observations alone but were interpolated in the regions where data were unavailable. There is uncertainty associated with the techniques used for

198 developing climatology. Due to the lack of seasonal data in some regions, the seasonality
199 shown in the data is significantly driven by the model used to interpolate. However, the
200 performance of the seasonality driven by the model used to derive climatology is tested using
201 pCO_2 data generated by the BOBOA buoy in the central BoB. Nevertheless, the observed
202 CO_2 fluxes carry several errors due to sparse coverage of data, wind speed measurements and
203 transfer velocity parameterizations and the uncertainty of the CO_2 fluxes is about 50%
204 (Gruber et al., 2009).
205
206 Since RECCAP1 (Sarma et al., 2013) important progress has been made on both pCO_2 data
207 delivery each year in the public domain for updating SOCAT data-product (www.socat.info,
208 Pfeil et al., 2013; Bakker et al., 2014, 2016) and the development of empirical methods that
209 reconstruct pCO_2 fields, including in synthesis studies (SOCOM project, Rödenbeck et al.,
210 2015). Here we used 9 empirical methods based on the SOCAT data (version v2020) and to
211 compare our new results with RECCAP1, we also used the original climatology of Takahashi
212 et al (2009) (Figure 1c). Recall that climatology was constructed for the reference year 2000
213 which would have to be taken into account when comparing pCO_2 fields for the recent year.
214 However, this would not dramatically impact the mean CO_2 fluxes assuming that over 1985-
215 2018 ocean pCO_2 increase is close to the atmospheric growth rate as observed in some parts
216 of the Indian Ocean (e.g. Metzl, 2009; Lauvset et al., 2015; Metzl et al., 2022; Lo Monaco et
217 al., 2021).
218
219 2.2.2. Ocean Hindcast models
220
221 CO_2 fluxes and surface water pCO_2 data were obtained from 12 GHM and 2 RHM (Table 1).
222 These models represent physical, chemical and biological processes controlling the marine

carbon cycling and exchange of CO_2 at the sea-to-atmosphere interface. The GHM have a coarse or an eddy-permitting horizontal resolution whereas RHM is eddy-resolving (Table 1). The simulations are forced with meteorological reanalysis products, given in Table 1. The models were run for different periods mostly between 1980 and 2019 with the period of each model given in Table 1. In order to make it uniform for all models, we have considered the runs between 1985 and 2018 in this study that gives the reference year of 2002. GHM and RHM have been integrated from the pre-industrial period to the present day with the same atmospheric CO_2 history. Although the model simulations were carried out following the RECCAP2 ocean modelling protocol, each model is different from others with respect to forcing, experimental configuration, representation of biogeochemical processes and sub-grid parameterizations (Table 1).

2.2.4. Atmospheric inversions

Atmospheric inversions (top-down) estimate the surface CO_2 fluxes based on the variability in the measured atmospheric CO_2 using an atmospheric transport model. In the atmospheric inversion models, a priori information about the surface CO_2 fluxes is used from bottom-up estimates (e.g., Takahashi et al., 2009) or an ocean GHM or an empirical upscaling model. In the Indian Ocean region and surrounding, atmospheric CO_2 measurements are available from only 8 sites that are used in the atmospheric inversion models. Among them, only two stations have long-record and others have short records. However, most inversions did not correct the oceanic prior fluxes significantly when the empirical upscaling model fluxes were used. Here we have chosen to show sea-air CO_2 fluxes from inversion models, one using prior flux from Takahashi et al. (2009) in the MIROC4-ACTM system (Chandra et al., 2022) and the other model (CAMSv20r1) using prior fluxes from an empirical model (Chevallier et

al., 2005). The atmospheric inversion model runs are available between 2001 and 2018 which gives the reference year of 2009.

2.2.5. Observation-based Surface pCO_2 (Empirical models)

Global sea-air CO_2 fluxes can also be estimated from pCO_2 measurements along the ship tracks over the past several decades. The first and simple upscaling method was implemented by Takahashi et al. (2009) where all the past measurements of CO_2 are separated in monthly-mean flux maps based on SST and salinity. This method relied on the extrapolation of Delta_pCO_2 data from limited measurements along the cruise tracks to the global ocean. With the development of neural networks and other artificial intelligence tools and organised archival of the SOCAT CO_2 database, several methods are now implemented to calculate gridded CO_2 flux including the interannual variation, taking into account the physical state of sea-surface conditions (Table 2; Rödenbeck et al., 2015: Landschützer et al., 2016; Fay et al., 2021). The estimated CO_2 fluxes between 1985 and 2018 were considered in this study with the reference year of 2002.

3. Results and Discussion

The simulations of CO_2 uptake by the Indian Ocean by GHM, RHM, empirical and atmospheric inversion models are compared with climatology with reference to (i) annual, (ii) seasonal and (iii) interannual timescales.

3.1. Annual mean CO_2 fluxes in the Indian Ocean between 1985 and 2018

273 3.1.1. Tropical Indian Ocean (north of the 37.5°S)

274

275 The annual mean sea-air CO_2 fluxes for 1985 to 2018 are presented in Table 3 and Figure 1d
276 for the entire Indian Ocean (37.5°S –30°N; 25-125°E), Arabian Sea (30-78°E and 0-30°N),
277 BoB (78-110°E and 0-30°N), EIO (30-125°E, 0-17°S) and SIO (37.5-17°S and 25-130°E).
278 The spatial variability in mean annual uptake for the entire Indian Ocean by GHM and RHM
279 (Figure 2), empirical (Figure 3) and atmospheric models (Figure 4) are given to evaluate the
280 spatial variability in CO_2 fluxes.

281

282 The simulated mean annual CO_2 sea–air fluxes by different models varied between -0.27 and
283 -0.13 PgC yr^{-1} for the Indian Ocean (Table 3), with a relatively lower sink estimated by
284 empirical models (-0.13±0.04 PgC yr^{-1}) than hindcast (-0.21±0.10 PgC yr^{-1}) and
285 atmospheric inversion models (-0.27±0.16 PgC yr^{-1}). Both hindcast and atmospheric
286 inversion models overestimated the sink of CO_2 by 3 times that of climatology (-0.07±0.14
287 PgC yr^{-1}) whereas empirical models are close to the observations. The observational pattern
288 of CO_2 flux shows that the SIO is a dominant sink whereas the Arabian Sea is a strong source
289 while EIO and the BoB are weak sources of atmospheric CO_2. All models simulated similar
290 patterns of spatial variations of the CO_2 fluxes (Figures 2 to 4) that are in agreement with
291 observations, but the magnitudes of fluxes are different. For instance, the modelled CO_2
292 fluxes were spread around the climatological values with relative overestimation of the sink
293 in the south of 22°S, in contrast, underestimation of the source was noticed by all models in
294 the north of 22°S in the Indian Ocean. In contrast, the RHM (both INCOIS-BIO-ROMS and
295 ROMS_NYUAD) reproduced CO_2 fluxes well in comparison with the climatology. Since the
296 ROMS_NYUAD model simulation was submitted up to 31.5°S only, we did not include it in
297 the SIO region as it was considered up to 37.5°S for other models. Similarly, the simulated

298 CO_2 fluxes by empirical models are in good agreement with the climatology (Figure 3). In the
299 case of the atmospheric inversions, a higher CO_2 sink in the south of 15^oS whereas sources of
300 CO_2 in the north of 15^oS than the observational climatology was observed (Figure 4). The
301 CO_2 fluxes by all models are in near perfect agreement with each other for the entire Indian
302 Ocean within the standard deviation of the estimates, however, they are different on the
303 regional subdivisions such as the Arabian Sea, BoB, EIO and SIO.
304
305 The standard deviation for the atmospheric inversion was large in the annual uptake (-
306 0.27±0.16 PgC yr^{-1}) while the smallest for the empirical models (-0.13±0.04 PgC yr^{-1}; Table
307 3). The highest standard deviation in the atmospheric inversion comes from the sparse
308 atmospheric CO_2 measurements, transport model uncertainties and differences in the prior
309 flux assumptions for the Indian Ocean. The atmospheric CO_2 time series data are available
310 only at 8 locations within the Indian Ocean resulting in high variability in the estimates. The
311 climatology also has a very high standard deviation (-0.07±0.14 PgC yr^{-1}) due to a lack of
312 enough data in the Indian Ocean as most of the Indian Ocean region is either sampled once or
313 twice and inter and extrapolation of the data (Takahashi et al., 2009).
314
315 The zonal integrated CO_2 fluxes by different models are given in Figure 5 and it shows that
316 most of the GHM underestimated CO_2 sink in the south of 25^oS whereas over estimated north
317 of 25^oS. The RHM (INCOIS-BIO-ROMS and ROMS_NYUAD) simulated exceptionally
318 well the zonal mean CO_2 fluxes in the Indian Ocean between 37.5^oS and 27.5^oN. However, a
319 slight underestimation was noticed for both the RHM and GHM in the north of 5^oN (Figure
320 5a). In the case of empirical models (Figure 5b), Jena-MLS, JMAMLR and UOEX_WAT20
321 were over-estimated in the south of 15^oS and well performed in the north of 15^oS with
322 reference to climatology. In the case of atmospheric inversions, a stronger sink is noticed in

the south of 15°S and a stronger source in the north of 10°S, compared to the empirical and hindcast models (Figure 5c).

Both spatial variations and zonal integration in the CO_2 fluxes (Figures 2-5) suggest that the model simulations significantly deviated from the climatology at several zones, namely the Oman/Somali upwelling region in the Arabian Sea, freshwater discharge region in the BoB, equatorial upwelling region and south equatorial current (SEC) and subtropical convergence zone regions in the southern tropical Indian Ocean. The potential reasons responsible for the regional variations in the CO_2 fluxes were discussed in detail below.

3.1.2. Northwestern Indian Ocean (Arabian Sea)

The Arabian Sea is simulated as a net source of CO_2 to the atmosphere by the hindcast models (0.006 to 0.058 PgC yr^{-1} with a mean of 0.03±0.01 PgC yr^{-1}), empirical models (0.052 to 0.098 with a mean of 0.08±0.01 PgC yr^{-1}) and atmospheric inversions (0.16±0.12 PgC yr^{-1}; Table 3) and it is consistent with the observations (Sarma, 2003; Goyet et al., 1998; Millero et al., 1998) and climatological fluxes (0.08±0.06 PgC yr^{-1}) (Table 3). Considering the standard deviation of climatology, and models, the mean of all modelled fluxes in the Arabian Sea (0.06±0.05 PgC yr^{-1}) is close to that of climatology (0.08±0.06 PgC yr^{-1}; Table 3). The large source of CO_2 to the atmosphere from the Indian Ocean is driven by the upwelling off Oman/Somali coasts, where pCO_2 levels as high as >600 µatm were reported during the peak southwest monsoon period (Körtzingeret al., 1997; Goyet et al., 1998; Sarma, 2003; Sabine et al., 2000). Most of the models poorly simulated CO_2 fluxes in the Oman/Somali upwelling region (Figures 2-4). Within the hindcast models, both MRI-ESM2-1 and ROMS_NYUAD models simulated CO_2 fluxes close to the observations (Figure 2).

348

349 The simulation of upwelling in the Arabian Sea may be a challenge due to the complex
350 interplay of winds, bottom topography, monsoonal circulation and mixing, to capture the
351 observed response by the models. The monsoon mixing is intense during summer (June to
352 September) resulting in high pCO_2 levels in the entire Arabian Sea with maximum off Oman
353 and Somalia coasts (Sarma et al., 1996; 1998; Goyet et al., 1998; Körtzinger et al., 1997). It
354 was estimated that the mixing effect is a dominant controlling factor of surface ocean pCO_2
355 in the Arabian Sea during the monsoon period while biological effect, mainly bacterial
356 degradation, dominates during the non-monsoon period (Louanchi et al., 1996; Sarma et al.,
357 2000). All hindcast models failed to simulate the monsoon mixing well resulting in weaker
358 fluxes of CO_2 (Figure 2) to the atmosphere. Since empirical models are mainly driven by
359 observations, they could simulate the impact of upwelling on pCO_2 reasonably well (Fig. 3).
360 In the case of atmospheric models, MACTM over-estimated coastal upwelling whereas
361 CAMSv20r1 remained close to that of the prior flux field from CEMES_LSCE_FFNN
362 (Figure 4). Sarma et al. (2013) noticed weak mixing in the GHM, and ocean inversion models
363 in the Arabian Sea between 1990 and 2009 and no improvements were noticed with reference
364 to mixing in the Arabian Sea in the past decade.
365

366 To examine the variability in the simulation of mixing in the Oman/Somalia upwelling
367 regions by different GHM and RHM, the sea surface temperature (SST) simulated by the
368 hindcast models was compared (Supplementary Figure S2). All models simulated upwelling
369 features off Oman/Somalia region, however, the intensity of mixing was different among
370 models, as reflected in the SST. It was noticed that mixing was weaker in CCSM-WHOI, EC-
371 Earth3, MOM6-Princeton, NorESM-OC1.2, ORCA025-GEOMAR and Planktom12 models
372 than in other GHM as former models showed relatively warmer SSTs than later models

compared to the climatology. Since a significant amount of data was contributed to the climatology from the Oman/Somali upwelling region, we can confidently attribute that the mixing and pCO_2 input from the subsurface layers in the Oman/Somalia upwelling region needs to be improved in the GHM for accurate simulations.

3.1.3. Northeastern Indian Ocean (Bay of Bengal)

All models simulated that the BoB is a mild source of CO_2 (0.00 to 0.01 PgC yr^{-1} with a mean of 0.00±0.01 PgC yr^{-1}) and it is consistent with the climatology (0.01±0.01 PgC yr^{-1}; Takahashi et al., 2009; Table 3). Sarma et al. (2012) reported that the peninsular river discharge increased the pCO_2 levels whereas glacial rivers (Ganges and Brahmaputra) discharge decrease the pCO_2 levels (Kumar et al., 1996; Mukhopadhyay et al., 2002). More recently Sarma et al. (2019) reported that cyclonic eddies enhance pCO_2 levels due to upwelling in the core of the eddy while anticyclonic eddies sink for atmospheric CO_2. Several recent investigations suggested that rapid acidification is being occurred in the BoB due to the deposition of atmospheric pollutants (Sarma et al., 2015; 2021; Kumari et al., 2022a,b) leading to an increase in pCO_2 levels. Unfortunately, neither GHM nor RHM has the atmospheric component to consider its impact.

Since river discharge enhances the CO_2 sink to the BoB, the differences in the sink of CO_2 in the BoB may be caused by variable use of river discharge data as this would influence the salinity of the upper ocean in the BoB. The existence of a strong linear relationship between salinity and pCO_2 levels was reported in the BoB (Kumar et al., 1996; Sarma et al., 2012; 2021). Recently, Sridevi and Sarma (2021) observed decreasing trends in surface pCO_2 levels due to a decrease in salinity over the past two decades due to the warming of Himalayan

398 glaciers (Goes et al., 2020). Therefore, salinity is a crucial parameter in controlling the pCO_2
399 levels in the BoB.
400
401 To examine this, the salinity simulations by different models were examined (Supplementary
402 Figure S3). All GHM simulated low salinity in the northern Bay but the magnitude of salinity
403 is different in the north of 15^{o}N. The lower salinity in the northern Bay was simulated in
404 CCSM-WHOI, MOM6-Princeton and ORCA1-LIM3-PISCES, whereas relatively high
405 salinity was simulated in CNRM-ESM2-1 and Planktom12. However, the sink in CO_2 was
406 observed in both high and low-salinity simulated models suggesting that variability in the
407 sink of CO_2 is not caused by river discharge/salinity in the GHM. An insignificant
408 relationship was observed between salinity and pCO_2 levels among different GHM and RHM
409 in the northern BoB (Figure is not shown) suggesting salinity or river discharge may not be a
410 controlling factor on variable CO_2 fluxes in the BoB. The absence of a relationship between
411 salinity and pCO_2 levels in the models suggests that the role of freshening surface waters by
412 rivers was not well constrained in the hindcast models.
413
414 3.1.4. Equatorial Indian Ocean (EIO)
415
416 The empirical models (0.02±0.02 PgC yr^{-1}) and atmospheric inversions models (0.02±0.03
417 PgC yr^{-1}) simulated a mild source of the atmospheric CO_2 and it is consistent with the
418 climatology (0.04±0.03 PgC yr^{-1}), in contrast, hindcast models estimated sink (-0.05± 0.04
419 PgC yr^{-1}) in the EIO. All models simulated that the western equatorial Indian Ocean is a
420 source whereas the eastern region is either a sink or close to balance. The higher sink
421 simulated by GHM is caused by weaker Somalia upwelling as discussed in section 3.1.2.
422 RHM simulated that the equatorial Indian Ocean is a mild source of atmospheric CO_2

(0.01±0.06 and 0.03±0.08 PgC yr^{-1} by ROMS-NYUAD and INCOIS-BIO-ROMS respectively). This can be noticed from the spatial distribution of SST, which is relatively warmer in the GHM in the western equatorial region compared to the RHM (Supplementary Figure S4) suggesting better simulation of upwelling in the RHMs. The spatial variations in CO_2 fluxes by RHM and atmospheric inversions (Figures 2 and 4) are consistent with the observations in the EIO region (Figure 1c).

3.1.5. The South Indian Ocean (SIO)

The SIO comprises two key oceanographic regimes of oligotrophic waters in the north and Southern Ocean waters in the south. These two regions are separated by the subtropical front (STF). We have considered the STF region as part of the SIO in this study. The estimated mean fluxes in this region by all models are -0.23±0.11 PgC yr^{-1} suggesting a strong sink of atmospheric CO_2 that agrees well with climatology (-0.20±0.16 PgC yr^{-1}; Table 3). The atmospheric inversions estimated a larger sink (-0.46±0.3 PgC yr^{-1}), which is mainly caused by MATCM whereas the CAMSv20r1 model performed well by staying close to the prior model. Despite atmospheric observations available in the SIO at Amsterdam Island at 38^{o}S, the overestimation of the sink by the atmospheric model must be examined. Both empirical models (-0.22±0.04 PgC yr^{-1}) and hindcast models, including RHM, (-0.20±0.07 PgC yr^{-1}) estimated CO_2 fluxes close to that of climatology (-0.22±0.04 PgC yr^{-1}). The CO_2 fluxes in the SIO are closer in magnitude to the annual uptake for the entire Indian Ocean (-0.19±0.1 PgC yr^{-1}) indicating that the majority of the net uptake of CO_2 occurs in the SIO, as suggested by other studies (Sabine et al., 2000; Bates et al., 2006; Metzl, 2009; Takahashi et al., 2009; Sarma et al., 2013).

448 The spatial variability in the magnitude of CO_2 flux within the SIO was variable among
449 hindcast models (Figure 2) in comparison to climatology (Figure 1c). For instance, the
450 climatology suggests a strong sink between 15^{o}S and 35^{o}S whereas the sink was simulated by
451 most of the hindcast models between 10^{o}S and 25^{o}S. Sabine et al. (1999) observed the highest
452 concentration and deepest penetration of anthropogenic carbon in the subtropical
453 convergence zone (30-40^{o}S). In contrast, a mild source is simulated by most of the models in
454 the south of 30^{o}S suggesting that the sink was underestimated in this zone. The outcropping
455 of these density surfaces and the subsequent sinking of surface waters provide a pathway for
456 excess CO_2 to enter the interior of the ocean. Overestimation of the CO_2 uptake by the
457 models in these zones suggests that vertical mixing was not constrained properly in the
458 models, leading to excess deep mixing, which increased surface water pCO_2 and a decrease in
459 the flux of the ocean (Figure 2).
460
461 3.2. Seasonal variations in pCO_2 levels and air-sea CO_2 fluxes in the Indian Ocean
462
463 To examine the seasonal variability of CO_2 fluxes by various modelling approaches, the
464 simulated surface pCO_2 levels and CO_2 fluxes were analysed (Figure 6). This provides
465 insights into the ability of the models to represent the complex interplay of physical and
466 biological processes on pCO_2 levels and sea-air CO_2 exchange. The ability of a model to
467 reproduce the seasonal cycle also provides some reassurance that the models are correctly
468 projecting climate sensitivity of the processes that could influence long-term projections of
469 the ocean CO_2 uptake (Fig. 6).
470
471 3.2.1. The Entire Indian Ocean
472

473 The increase in pCO_2 levels is expected in the tropical Indian Ocean between June and
474 September due to an increase in mixing driven by the southwest monsoon in the north
475 whereas deeper mixing in the SIO (Louanchi et al., 1996; Sarma et al., 2000; Sabine et al.,
476 2000; Bates et al., 2006). All hindcast models overestimated the sink between June and
477 September but were close to observation during other months (Fig. 6) due to weak mixing of
478 pCO2-rich subsurface waters with surface. Among the other models, ROMS-NYUAD and
479 MPIOM-HAMOCC displayed relatively better seasonality in CO_2 fluxes compared to
480 climatology (Figure S5). The mean empirical models followed seasonality close to that of
481 observations. The atmospheric inversions overestimated the sink from March to October
482 mainly in the SIO compared to other models and climatologySince the seasonality in CO_2
483 fluxes is variable with space, the same in different regions of the Indian Ocean are examined.
484
485 3.2.2. Northwestern Indian Ocean (Arabian Sea)
486
487 The Arabian Sea shows strong seasonality with higher CO_2 fluxes from June to September
488 associated with monsoon mixing and high winds compared to other seasons (George et al.,
489 1994; Sarma et al., 1996; 1998; Sarma, 2003). The climatological amplitude of seasonality
490 was close to 0.2 PgC yr^{-1} with a maximum in June-August and a minimum in October-
491 December (Figure 6). The seasonality was perfectly captured by the empirical models
492 whereas atmospheric inversion and hindcast models failed to simulate as they over and
493 underestimated respectively. Though atmospheric inversion models mostly captured the high
494 CO_2 fluxes to the atmosphere from June to August but with a large spread compared to other
495 simulations by hindcast and empirical models. In contrast, hindcast models showed a
496 response but it was strongly out of phase with the observations by giving maximum fluxes in
497 May to June and minimum fluxes in July to September with approximately 3-4 months ahead

498 of the climatological peak in CO_2 fluxes. The two GHM (MRI-ESM2-1 and NorESM-OC1.2)
499 and RHM (ROMS-NYUAD) simulated peak fluxes between June and August in the Arabian
500 Sea (Figure S5).
501
502 All GHM failed to simulate seasonality in pCO_2 (Figure 6) levels as the higher pCO_2 levels
503 were observed during July to September in the observations whereas April to May in the
504 models. High pCO_2 levels were reported from June to August due to enhanced vertical
505 mixing caused by monsoon winds in the Arabian Sea (Sarma et al., 1996; 1998; Körtzinger et
506 al., 1997; Millero et al., 1998; Sarma, 2003). Sarma et al. (2000) observed that mixing is the
507 dominant controlling factor of pCO_2 levels from June to August in the Arabian Sea followed
508 by biological effects (Louanchi et al., 1996; Goyet et al., 1998). The difference in pCO_2
509 levels between mean hindcast models and observations varied between 15 and 50 μatm
510 whereas it was <20 μatm in the case of empirical models (Figure 6). The reference year for
511 climatology is 2000 (Takahashi et al., 2009) whereas the reference year for hindcast and
512 empirical models are 2002 (1985-2018). The difference in pCO_2 levels caused by variable
513 reference year may differ up to 4 μatm considering the 2 μatm/y as a growth rate of surface
514 ocean pCO_2 (Metzl, 2009) suggesting that weaker mixing in the models underestimated the
515 seasonality in pCO_2 and CO_2 fluxes in the Indian Ocean.
516
517 3.2.3. Northeastern Indian Ocean (Bay of Bengal; BoB)
518
519 The BoB also displayed large seasonality with higher CO_2 fluxes from May to August
520 associated with monsoon mixing and decreased between October and December due to river
521 discharge and stratification (Figure 6; Sarma et al., 2016; 2018; 2019). All models simulated
522 high CO_2 fluxes during May but decreased to low by July-August (Figure 6). The observed

amplitude of seasonality was close to 0.02 PgC yr^{-1} with the maximum in May-June (0.02 PgC yr^{-1}) and minimum in February (0 PgC yr^{-1}). The mean hindcast models simulated similar amplitude (0.02 PgC yr^{-1}) but they showed sink (0 and -0.02 PgC yr^{-1}) instead of source in the climatology. The atmospheric inversion models displayed too low (high sink during February) and high source from August to October.

All GHM simulate seasonality in pCO_2 levels in the BoB with a maximum in April and May and a minimum in February (Figure 6). The magnitude of seasonal variability in pCO_2 is ~15 µatm in the climatology whereas hindcast models simulated 15-40 µatm with lower variability (<20 µatm) during April and May and higher (>35 µatm) during other months. The underestimation of pCO_2 in the BoB may be caused by strong stratification in the model leading to lower input from pCO_2-rich subsurface waters. In addition to this, the difference between simulations and observation may also be caused by the lack of enough data in the observations as the BoB is severely under-sampled with reference to seasons. To resolve this issue, the pCO_2 data collected by the BOBOA mooring buoy in the central BoB (Figure 1a) is used for comparison. This buoy collected data between 2013 and 2018 (Sutton et al 2019) and the monthly climatology of this data was compared with Takahashi climatology. The BOBOA climatology showed an increase in pCO_2 starting in April with a peak in May whereas Takahashi climatology displayed during April suggesting that Takahashi climatology well reproduced the observed seasonality although the climatology was not constrained with BOBOA data. Most of the hindcast models displayed peaks in April-May in the BoB and were also consistent with the climatology (Figure S5).

3.2.4. Equatorial Indian Ocean (EIO)

548 The CO_2 fluxes in the EIO displayed seasonality with high fluxes from January to May and
549 low from June to October with a minimum in August (Figure 6). The mean observed CO_2
550 fluxes are the source of the atmosphere during all seasons whereas all hindcast models
551 simulated sink, especially between May and November. All models displayed similar
552 seasonal variability in CO_2 fluxes but underestimated from May to November. The RHM
553 simulated better seasonality in the CO_2 fluxes compared to GHM (Figure S5).
554
555 The EIO displays relatively weak pCO_2 seasonality with a high from February to April and a
556 low from June to October. The amplitude of seasonality in pCO_2 was <10 μatm in the
557 climatology. All models simulated the seasonality but they were under-estimated pCO_2 by
558 ~20 μatm from that of climatology (Figure 6).
559
560 3.2.5. The South Indian Ocean (SIO)
561
562 The SIO displayed large seasonality in fluxes with CO2 source during January to March and
563 CO2 sinks during other months (Figure 6). All models reproduced seasonality very well in
564 the SIO (Figure S5).
565
566 All GHM simulate seasonality in pCO_2 levels in the SIO with a maximum in January and
567 March and a minimum in July-August. The magnitude of seasonal variability in pCO_2 is ~15
568 μatm in the climatology whereas hindcast models simulated <20 μatm. The difference in
569 pCO_2 between simulation and observations was up to 40 μatm (Figure S5). The large
570 difference in pCO_2 seasonality in the SIO may be caused by weaker mixing simulations in the
571 models in austral winter and the opposite in summer.
572

573 3.3. Interannual variability (IAV)

574

575 The interannual variability and trends in pCO_2 levels and their fluxes at the air-water
576 interface was also investigated in 1985-2018 using different models (Figure 7). The rate of
577 increase in surface ocean pCO_2 levels varied from 1.54 to 1.73 μatm yr^{-1} between 1985 and
578 2018 with a lower rate of increase in the BoB and higher in the EIO and SIO. The growth rate
579 of pCO_2 in the surface waters by both hindcast and empirical models is close to that of
580 atmospheric growth and observed surface pCO_2 growth in the Southwestern Indian Ocean
581 (Metzl, 2009; Lo Monaco et al., 2021; Leseurre et al., 2022). Due to the lack of basin-scale
582 observational time-series data in the Indian Ocean, the performance of the IAV by the models
583 cannot be assessed. Given the variability of IOD and ENSO index (Figure 7), we divided the
584 IAV trends into three timelines, i.e., a) 1985-2000, b) 2001-2018 and c) 1985 to 2018 (Figure
585 7; Tables 4 and 5) to examine the possible changes in growth rate in the recent decades from
586 that of earlier. To avoid biasing the magnitude of the seasonality, we first de-trend the
587 simulated time series of IAV.

588

589 3.3.1. The entire Indian Ocean

590

591 Both hindcast and empirical models simulated IAV in the surface pCO_2 levels in the entire
592 Indian Ocean as 1.67 to 1.70 μatm yr^{-1} between 1985 and 2018. The rate of increase in pCO_2
593 levels was lower from 1985 to 2000 (1.41-1.49 μatm yr^{-1}) and increased in the recent decades
594 (2001-2018) to 1.84-1.96 μatm yr^{-1} (Table 4). Within the variability in the estimations, both
595 empirical and hindcast models simulated similar growth rates in pCO_2 levels (Figure 7).

596

The range of sea-to-air CO_2 fluxes for the period of 1985 to 2018 was significantly different for GHM (-0.48 to -0.06 PgC yr^{-1}), empirical (-0.31 to 0.03 PgC yr^{-1}) and atmospheric inversion models (-0.63 to 0.09 PgC yr^{-1}) (Figure 7). The IAV trend between 1985 and 2018 was close for hindcast (-0.023±0.003 PgC yr^{-1} $decade^{-1}$) and empirical models (-0.021±0.003 PgC yr^{-1} $decade^{-1}$; Table 5). The trends in IAV by hindcast models between 2001 and 2018 (-0.023±0.007 PgC yr^{-1} $decade^{-1}$) were slightly lower compared to 1985-2000 (-0.028±0.012 PgC yr^{-1} $decade^{-1}$) for the entire Indian Ocean suggesting the rate of sinking of CO_2 in the Indian Ocean is decreasing in the recent decades. In contrast, empirical models displayed larger IAV between 2001-2018 (-0.046±0.005 PgC yr^{-1} $decade^{-1}$) and 1985-2000 (+0.007±0.007 PgC yr^{-1} $decade^{-1}$). Such differences in the empirical models may come from the lack of satellite Chl-a data before 1998. Therefore, the simulations of empirical models may be less accurate before 1998 than after. Interestingly IAV by empirical models during 2001-2018 were more than double (-0.046±0.005 PgC yr^{-1} $decade^{-1}$) than that of hindcast models (-0.023±0.007 PgC yr^{-1} $decade^{-1}$) which may be driven by variability in wind products and transfer velocity coefficients used. To examine the spatial variability in IAV, the same is studied in different regions of the Indian Ocean.

3.3.2. Northwestern Indian Ocean (Arabian Sea)

The pCO_2 growth of 1.64 to 1.68 µatm yr^{-1} was simulated between 1985 and 2018 and it was lower during 1985-2000 (1.32-1.41 µatm yr^{-1}) than 2001-2018 (1.76-1.88 µatm yr^{-1}) (Table 4) in the Arabian Sea. The growth rates in pCO_2 levels in the Arabian Sea are close to that of the atmospheric growth rate of CO_2 (WMO Bulletin; https://gml.noaa.gov/ccgg/trends/).

The IAV in the CO_2 fluxes by the hindcast models in the Arabian Sea was small (0.00 to 0.06 PgC yr^{-1}), it was larger than the mean flux to the atmosphere from 1985 to 2018 (0.03±0.01 PgC yr^{-1}). This suggests that the mean CO_2 flux to the atmosphere may vary significantly from year to year (Figure 7).. In contrast, the atmospheric inversions (for the period 2001-2018) gave a much larger standard deviation than hindcast models suggesting that about 50% of the total Indian Ocean variability occurs in the NIO. The high variability in the atmospheric inversions may come from the period and region of atmospheric CO_2 data used in the models. The empirical models estimated lower IAV (0.03 to 0.12 PgC yr^{-1}) compared to hindcast and atmospheric inversion models.

To examine the IAV trends in the recent decades, the trends between 1985-2000 and 2001-2018 were compared. The IAV between 2001-2018 is lower (-0.005±0.002 PgC yr^{-1} $decade^{-1}$) than 1985-2000 (-0.001±0.002 PgC yr^{-1} $decade^{-1}$) by hindcast models suggesting that the source of the CO_2 to the atmosphere from the Arabian Sea is decreasing in the recent decades. This is possible that rapid warming of the western Arabian Sea was reported in recent decades (Roxy et al.,2015; Sridevi et al., 2023) resulting in weak vertical transport of CO_2, and nutrients resulting in a decrease in primary production (Dunstan et al., 2018; Roxy et al., 2016; Sridevi et al., 2023). A decline in Somali upwelling intensity and decreased evaporation due to the weakening of winds led to the warming of the Indian Ocean was reported in recent decades (D'Mello and Prasanna Kumar (2018). Sarma et al. (2000) estimated that vertical mixing is the major contributor to high pCO_2 levels and fluxes to the atmosphere in the Arabian Sea. The decrease in mixing may also weaken primary production resulting in an increase in CO_2 flux. Recently Sridevi et al. (2023) found that net primary production was decreasing only in the southern Arabian Sea (south of $12^{o}N$) whereas the decrease in nutrient inputs through mixing is compensated by increased atmospheric

deposition of nutrients. Therefore, the weakening of upwelling intensity decreased the CO_2 source to the atmosphere in the past 4 decades in the Arabian Sea. The empirical models also simulated a decrease in the CO_2 fluxes from -0.002±0.002 PgC yr^{-1} $decade^{-1}$ in 1985-2000 to -0.011±0.001 PgC yr^{-1} $decade^{-1}$ in 2001-2018 and the magnitude of the decrease is higher than hindcast models. Nevertheless, this analysis suggests that the source of CO_2 to the atmosphere from the Arabian Sea is decreasing due to the warming of the basin leading to stratification and a decrease in upwelling intensity in the western basin.

3.3.3. Northeastern Indian Ocean (Bay of Bengal; BoB)

The IAV trends of pCO_2 simulated by hindcast and empirical models were close (1.54±0.04 and 1.64±0.02 μatm yr^{-1} respectively) between 1985 and 2018 in the BoB and these rates are almost close to that of in the Arabian Sea (Table 4). The pCO_2 growth rate increased between 1985 and 2000 (1.34-1.46 μatm yr^{-1}) to 2001-2018 (1.71-1.76 μatm yr^{-1}; Table 4) and it is consistent with the atmospheric growth rate (https://gml.noaa.gov/ccgg/trends/).

The IAV in the BoB simulated by the hindcast models is small (-0.02 to +0.02 PgC yr^{-1}), and it is larger than the mean flux to the atmosphere from 1985 to 2018 (0.00±0.02 PgC yr^{-1}). This suggests that the mean CO_2 flux to the atmosphere may vary from a net weak sink to a weak source to the atmosphere. The standard deviation is large suggesting that large IAV occurs in the BoB. In contrast, the atmospheric inversions showed a large standard deviation in comparison to hindcast models suggesting high IAV could occurs in the BoB (-0.03 to +0.04 PgC yr^{-1}). On the opposite the empirical models showed low IAV in CO_2 fluxes (0.00 to 0.02 PgC yr^{-1}) and it is close to that of the annual mean flux to the atmosphere

(0.01±0.005 PgC yr^{-1}; Table 3). The empirical models estimated very low IAV compared to hindcast and atmospheric inversion models in the BoB (Figure 7).

The IAV in the CO_2 fluxes in the BoB from the hindcast models decreased from 1985-2000 (-0.002±0.002 PgC yr^{-1} $decade^{-1}$) to 2001-2018 (-0.005±0.001 PgC yr^{-1} $decade^{-1}$) but not statistically different. (Table 5). Similarly, empirical models simulated a decrease in the fluxes of CO_2 in the BoB in recent decades (Table 5). The decrease of the CO2 sink may be potentially caused by the deposition of atmospheric pollutants. Recently Sridevi and Sarma (2021) analyzed long-term trends (1998-2015) in pCO_2 levels in the BoB using an empirical model and noticed that pCO_2 decreased at the rate of -0.1 to -2.9 µatm yr^{-1} in the central and eastern Bay associating with the decrease in salinity. The decrease in salinity is manifested by the melting of Himalayan glaciers due to climate change (Goes et al., 2020). In contrast, an increase in pCO_2 levels was noticed in the head bay and western BoB (0.1 to 2.4 µatm yr^{-1}) due to the deposition of atmospheric pollutants (Sarma et al., 2015; 2022). Therefore the decrease in the rate of CO_2 flux from the atmosphere in the recent decade may be caused by a decrease in salinity and deposition of atmospheric pollutants in the BoB.

3.3.4. Equatorial Indian Ocean (EIO)

The pCO_2 simulations displayed significant IAV by hindcast and empirical models in the equatorial Indian Ocean (1.65-1.72 µatm yr^{-1}) between 1985 and 2018. The enhanced pCO_2 growth rate was observed during the recent decade (2001-2018; 1.52-2.01 µatm yr^{-1}; Table 4) than between 1985 and 2000 (1.43-1.52 µatm yr^{-1}). The IAV in the CO_2 fluxes in the EIO simulated by the hindcast models is small (-0.11 to 0.06 PgC yr^{-1}), and it is larger than the mean flux to the atmosphere from 1985 to 2018 (-0.03±0.05 PgC yr^{-1}). The large standard

695 deviation in the IAV by hindcast models suggested large variations in the CO_2 fluxes in the
696 EIO and the mean CO_2 flux to the atmosphere may vary between weak sink to the source to
697 the atmosphere. In contrast, both empirical and atmospheric inversion models displayed a
698 decrease in the source for the past three decades. The hindcast models displayed a rate of
699 decrease in CO_2 fluxes from the EIO between 1985-2000 (-0.004±0.005 PgC yr^{-1} $decade^{-1}$)
700 to 2001-2018 (-0.006±0.003 PgC yr^{-1} $decade^{-1}$) whereas a decrease was also noticed by
701 empirical models but the magnitude was higher (+0.01±0.003 and -0.018±0.002 PgC yr^{-1}
702 $decade^{-1}$ during 1985-2000 and 2001-2018 respectively). This analysis suggests that the CO_2
703 sink in the EIO is increasing in recent decades possibly due to the weakening of upwelling in
704 the western basin due to rapid warming (D'Mello and Prasanna Kumar, 2018; Roxy et al.,
705 2015) leading to less DIC import in surface.
706
707 3.3.5. The South Indian Ocean (SIO)
708
709 The IAV of pCO_2 simulated by hindcast and empirical models in the SIO were close
710 (1.73±0.03 and 1.70±0.02 µatm yr^{-1} respectively) between 1985 and 2018. The lower pCO_2
711 growth rate was observed between 1985 and 2000 (1.43-1.50 µatm yr^{-1}) while increased in
712 the recent decades of 2001-2018 (1.91-1.98 µatm yr^{-1} (Table 4). A slight increase in the
713 surface ocean pCO_2 growth rate from north (Arabian Sea; 1.88±0.06 µatm y^{-1} between 2001-
714 2018) to SIO (1.98±0.05 µatm y^{-1}) was observed in the hindcast models whereas such trends
715 were not noticed in the empirical models (Table 4). In the period 1991–2007, Metzl (2009)
716 calculated an oceanic pCO_2 growth rate of 2.11±0.11 µatm yr^{-1}, which is 0.4 µatm yr^{-1} faster
717 than in the atmosphere, suggesting that this region acts as a reducing sink of atmospheric
718 CO_2. Recently Lo Monaco et al. (2021) reported increasing trends of pCO_2 in the southern
719 Mozambique Channel ranging from 1.14 µatm yr^{-1} from1963 to 1995, 1.70 µatm yr^{-1} from

720 1995 to 2004 and 2.41 μatm yr^{-1} from 2004 to 2019, and these rates are close to that of
721 atmospheric CO_2 trend. The growth rate of pCO_2 estimated by both hindcast and empirical
722 models appears close to that of measured values in the SIO (Metzl, 2009; Lo Monaco et al.,
723 2021; Leseurre et al., 2022).
724
725 The IAV in the SIO by the hindcast models is small (-0.41 to -0.03 PgC yr^{-1}), and it is larger
726 than the mean flux to the atmosphere from 1985 to 2018 (-0.03±0.05 PgC yr^{-1}). The large
727 standard deviation in the IAV by hindcast models suggested large variations in the CO_2
728 fluxes in the SIO and the mean CO_2 flux to the atmosphere may vary between weak sink to
729 the source to the atmosphere. In contrast, the empirical model did not show large variability
730 but atmospheric inversion models displayed large standard deviations (Figure 7) with a
731 higher increase in the sink from -0.4 to -0.45 PgC yr^{-1} between 2001 and 2018. The hindcast
732 models displayed a decrease in CO_2 fluxes from the SIO between 1985-2000 (-0.02±0.006
733 PgC yr^{-1} $decade^{-1}$) to 2001-2018 (-0.006±0.005 PgC yr^{-1} $decade^{-1}$) whereas a decrease was
734 also noticed by empirical models but the magnitude was higher (-0.003±0.005 to -
735 0.012±0.004 PgC yr^{-1} $decade^{-1}$ during 1985-2000 and 2001-2018 respectively).
736
737 3.4. Role of climate variability on CO_2 flux
738
739 The IAV in sea-air CO_2 fluxes in the Indian Ocean has been linked to the IOD and ENSO.
740 Valsala and Maksyutov (2013) reported a strong correlation between the IODZM and sea-air
741 CO_2 flux IAV in the Arabian Sea and that the roles of these two (ENSO and IODZM) modes
742 are complementary in the period 1985-2018. The strong IOD event occurred in 1994, 1997
743 and 2006 within the period considered in this study with a Dipole Mode Index (DMI) value
744 >0.6. The simulated IAV by hindcast models shows an annual mean higher CO_2 flux during

745 1994, 1997 and 2006 by 9-14% in the Arabian Sea whereas a decrease by 5-30% was noticed
746 in other regions (BoB; EIO and SIO) than in adjacent years. This is consistent with earlier
747 observations (Sarma, 2006; Valsala and Maksyutov, 2013). Interestingly, empirical models
748 displayed an increase in CO_2 fluxes by 8% in 1994 but a decrease in flux by 10% was noticed
749 between 1997 and 2006 compared to the normal period in the Arabian Sea. In contrast, a
750 significant increase in CO_2 fluxes in the EIO by 3 to 45% was simulated by empirical models
751 whereas a decrease of 6-30% was simulated by hindcast models. Jabaud-Jan et al. (2004)
752 noticed sea-to-air fluxes in the subtropical zone (20^oS-37^oS) associated with warming in
753 January 1998, when strong IOD occurred, compared to sink observed in the same region
754 during 2000 suggesting warming induced by IOD enhanced CO_2 fluxes to the atmosphere.
755 However, neither hindcast nor empirical models captured these features. The monthly mean
756 CO_2 fluxes simulated by hindcast and empirical models in the Indian Ocean, including in the
757 Arabian Sea, did not show significant relation with Dipole Mode Index (DMI) between 1985
758 and 2018 suggesting that weak IOD may not have a significant impact on CO_2 fluxes in the
759 Indian Ocean.
760
761 The strong ENSO event (index value >1.0) occurred in 1987, 1992, 1997, 2010 and 2016
762 within the period considered in this study. During these events increase in annual mean CO_2
763 fluxes by 6-26% was observed in the Arabian Sea and BoB whereas a decrease in CO_2 fluxes
764 was noticed in the EIO and SIO by hindcast models. In contrast, empirical models showed a
765 decrease in CO_2 fluxes in the ENSO years in the Arabian Sea, BoB and SIO but an increase
766 in the EIO. The monthly ENSO index displayed a significant linear correlation with CO_2
767 fluxes by hindcast models in the Arabian Sea and BoB ($p<0.001$) but an insignificant
768 relationship in the EIO and SIO ($p>0.01$ and $p>0.1$ respectively) whereas insignificant
769 relation was observed with CO_2 fluxes by empirical models in all regions. Valsala and

Maksyutov (2013) found a positive relationship between the ENSO index and CO_2 fluxes in the Arabian Sea and Southern Peninsular India. Nevertheless, this study suggests that empirical models did not capture either ENSO or IOD impacts on the CO_2 fluxes in the Indian Ocean.

Significant negative anomalies in the CO_2 fluxes were reported in the tropical Indian and Pacific Oceans and the absence of such anomaly was reported in the Southern Ocean (McKinley et al., 2020; Bennington et al., 2022). Bennington et al. (2022) reported an increase in >30% of the sink after the Pinatubo eruption. Interestingly significant decrease in CO_2 flux was observed between 1991 and the mean of 1992-93 in the Arabian Sea (0.038 and 0.032 PgC/y respectively), BoB (0.0033 and 0.002 PgC/y), EIO (-0.026 and -0.041) with decrease by 16 to 57% whereas it was smaller in the case of SIO (-0.18 and -0.19 PgC/y) associated with Pinatubo volcanic eruption (Fig. 7). These observations are consistent with the earlier studies (McKinley et al., 2020; Bennington et al., 2022). Recently Fay et al. (2023) reported high oxygen and carbon anomalies associated with Pinatubo volcanic eruptions for several years in the northern and tropical Pacific and tropical Indian Ocean but an insignificant impact is noticed in the Southern Ocean. The models used in this study also suggest an impact of the Pinatubo volcanic eruption on Indian Ocean CO_2 fluxes around 1991-1992 most pronounced in the EIO region (Fig. 7).

4. Conclusions

The Indian Ocean is severely under-sampled with reference to surface pCO_2 levels. In order to estimate the uptake of CO_2 by the Indian Ocean, CO_2 fluxes were simulated using several approaches, such as a) hindcast, b) atmospheric inversions, and c) empirical models, were

795 analyzed at different time scales and compared with spatially interpolated observations
796 (called climatology). Our study suggests that the annual mean CO_2 uptake by the entire
797 Indian Ocean (north of 37.5^{o}S) from all approaches varied between -0.27 and -0.13 PgC yr^{-1}
798 with a mean value of all models of -0.19±0.01 PgC yr^{-1}. The SIO (south of 18^{o}S) region is a
799 dominant annual sink for the atmospheric CO_2 with a mean of all models of -0.23±0.11 PgC
800 yr^{-1}. In contrast, a mild source of CO_2 in the atmosphere was simulated by all models
801 (0.02±0.05 PgC yr^{-1}) in the north of 18^{o}S. The estimation of CO_2 uptake by the Indian Ocean
802 was shown little variations among models.
803
804 All models simulated spatial variability in CO_2 fluxes in the Indian Ocean except for the
805 underestimation of upwelling fluxes off Oman/Somalia coasts, and the EIO and
806 overestimation of sink in the BoB due to poor monsoon mixing and freshwater discharge
807 simulations in the hindcast models. The RHM have improved the simulation of CO_2 fluxes,
808 compared to GHM, in these regions but has not reached close to the climatology. Variations
809 in CO_2 fluxes by different models were also driven by variations in wind products, transfer
810 velocity parameterization and atmospheric CO_2 data used in the flux estimations.
811
812 The atmospheric growth rate of pCO_2 was well simulated by all models and they captured the
813 seasonal cycle in the sea-air CO_2 fluxes, however, the stronger amplitudes were simulated by
814 all models than climatology. The empirical models simulated the seasonal cycle of sea-air
815 CO_2 fluxes reasonably well with the observations. The difference between the hindcast and
816 atmospheric inversion models and also in comparison with climatology may reflect errors in
817 the model formulations and also poor observational data both in the atmosphere and ocean
818 surface.
819

The inter-annual variability in CO_2 fluxes by the hindcast models is relatively weaker compared to the atmospheric inversions. The hindcast models suggest a slight weakening of the sink over the period of 1985-2018 in the SIO. In contrast, a decrease in the source of CO_2 in the atmosphere was simulated in the Arabian Sea, BoB and EIO by the hindcast and empirical models. It is difficult to conclude how models are performing about IAV due to the lack of time-series atmospheric and surface ocean pCO_2 observations. All models projected the influence of atmospheric extreme events, such as IODZM and ENSO on CO_2 fluxes in the Indian Ocean.

Unless the monsoon mixing is represented well in the models, it will remain difficult to confidently project the future changes in CO_2 fluxes in the Indian Ocean. The lack of seasonal data in most parts of the Indian Ocean is another serious problem to validate the models. Significant improvement in model performance was not noticed since the RECCAP1 comparison between models and observations due to the lack of addition of new data in this region (Sarma et al., 2013). Therefore, intensive ocean observations of pCO_2 and atmospheric tower observations are required for further improvements of the models.

The Indian Ocean experiences extreme events such as eddies (Chen et al., 2012) and tropical cyclones and both cause enormous effluxes of CO_2 to the atmosphere that would influence local CO_2 fluxes (Byju and Prasanna Kumar, 2011; Ye et al., 2019). Swapna et al. (2022) projected an increase in cyclonic activity in the future in the Indian Ocean that may result in enhanced CO_2 fluxes at the air-sea interface. High resolution, with reference to space and time, is required to capture such features. The regional models are highly useful to capture such signatures than global models. It would be interesting to segregate the contribution of CO_2 fluxes due to an increase in cyclonic activity due to climate change.

Rapid warming of the Indian Ocean (Roxy et al., 2015) is experiencing and began to play an important role in global ocean heat uptake (Li et al, 2018). The decrease in the rate of warming due to aerosols was reported in the northern Indian Ocean (Sridevi et al., 2023). The decrease in the primary production in the western Indian Ocean (Roxy et al., 2016; Dalpadado et al., 2021; Sridevi et al., 2023), was reported due to the decline in wind speed and upwelling intensity. The lack of primary productivity trends due to an increase in the deposition of nutrients from the atmosphere was reported (Sarma et al., 2022; Sridevi et al., 2023). Rapid rate of ocean acidification was reported due to the atmospheric deposition of pollutants (Sarma et al., 2015; 2021; Kumar et al., 2022). Therefore the inclusion of atmospheric pollutants in the model improves the simulations of future changes in CO_2 fluxes significantly. Evaluating the changes in possible drivers due to climate change would be an interesting issue to look into in the future.

One serious drawback in the present study to use of observational climatology of CO_2 fluxes to compare with the model simulations. Due to a lack of observational data in the Indian Ocean, inter and extrapolations were done based on the advection-diffusion model (Takahashi et al., 2009). Recently Davis and Goyet (2021) suggested a new method to fill the gaps to balance the error in the undersampled regions. Utilizing such tools, as shown by Guglielmi et al. (2022 a, b), may further decrease errors associated with climatology and the evaluation of model simulations will be enhanced.

Acknowledgement: We would like to thank all the modellers who have supplied the model outcomes to perform this analysis. The RECCAP2 organizers are also thanked for organizing the meeting in Japan and also simulating discussions over the online platform to perform this exercise, especially Drs. Jensdaniel Mueller, Nicolas Gruber. NC is supported by the Arctic

Challenge for Sustainability phase II (ArCS-II; JPMXD1420318865) Projects of the Ministry of Education, Culture, Sports, Science and Technology (MEXT). PKP is partly supported by the Environment Research and Technology Development Fund (JPMEERF21S20800) of the Environmental Restoration and Conservation Agency of Japan. The INCOIS-BIO-ROMS regional Indian Ocean model has been configured as a part of the 'Development of Climate Change Advisory Services' project of the Indian National Centre for Ocean Information Services (INCOIS) under the 'Deep Ocean Mission' programme of the Ministry of Earth Sciences (MoES). This is INCOIS contribution number XXX. ZL is supported by Tamkeen through Research Institute grant CG009 to the NYUAD Arabian Center for Climate and Environmental Sciences (ACCESS). The Surface Ocean CO_2 Atlas (SOCAT, www.socat.info) used for empirical models is an international effort, endorsed by the International Ocean Carbon Coordination Project (IOCCP), the Surface Ocean Lower Atmosphere Study (SOLAS) and the Integrated Marine Biogeochemistry and Ecosystem Research program (IMBER), to deliver a uniformly quality-controlled surface ocean CO2 database. We thank the two anonymous reviewers for making constructive suggestions, which resulted in improvements to this paper. This is NIO contribution number …..

889 References

890 Al Azhar, M., Lachkar, Z., Lévy, M., & Smith, S. (2017). Oxygen minimum zone contrasts
891 between the Arabian Sea and the Bay of Bengal implied by differences in remineralization
892 depth. Geophysical Research Letters, 44(21), 11-106.

893 Bakker, D. C., Pfeil, B., Landa, C. S., Metzl, N., O'brien, K. M., Olsen, A., et al. (2016). A
894 multi-decade record of high-quality fCO 2 data in version 3 of the Surface Ocean CO 2 Atlas
895 (SOCAT). *Earth System Science Data*, *8*(2), 383-413.

896 Bakker, D. C., Pfeil, B., Smith, K., Hankin, S., Olsen, A., Alin, S. R., et al. (2014). An update
897 to the Surface Ocean CO 2 Atlas (SOCAT version 2). *Earth System Science Data*, *6*(1), 69-
898 90.

899 Bakker, D. C. E., Alin, S. R., Bates, N., Becker, M., Castaño-Primo, R., Cosca, C. E., et al.
900 (2020). Surface Ocean CO2 Atlas Database Version 2020 (SOCATv2020)(NCEI accession
901 0210711). *NOAA National Centers for Environmental Information. Doi*.org/10.25921/4xkx-
902 ss49. 2020.

903 Bates, N. R., Pequignet, A. C., & Sabine, C. L. (2006). Ocean carbon cycling in the Indian
904 Ocean: 1. Spatiotemporal variability of inorganic carbon and air-sea CO2 gas
905 exchange. *Global Biogeochemical Cycles*, *20*(3).

906 Behrenfeld, M. J., & Falkowski, P. G. (1997). Photosynthetic rates derived from satellite-
907 based chlorophyll concentration. *Limnology and oceanography*, *42*(1), 1-20.

908 Bennington, V., Gloege, L., & McKinley, G. A. (2022). Variability in the global ocean
909 carbon sink from 1959 to 2020 by correcting models with observations. *Geophysical*
910 *Research Letters*, *49*(14), e2022GL098632.

911 Bettencourt, J. H., López, C., Hernández-García, E., Montes, I., Sudre, J., Dewitte, B., et al.
912 (2015). Boundaries of the Peruvian oxygen minimum zone shaped by coherent mesoscale
913 dynamics. *Nature Geoscience*, 8(12), 937-940.

914 Bopp, L., Resplandy, L., Orr, J. C., Doney, S. C., Dunne, J. P., Gehlen, M., ... &Vichi, M.
915 (2013). Multiple stressors of ocean ecosystems in the 21st century: projections with CMIP5
916 models. *Biogeosciences*, 10(10), 6225-6245.

917 Brandt, P., Bange, H. W., Banyte, D., Dengler, M., Didwischus, S. H., Fischer, T., et al.
918 (2015). On the role of circulation and mixing in the ventilation of oxygen minimum zones
919 with a focus on the eastern tropical North Atlantic. *Biogeosciences*, 12(2), 489-512.

920 Byju, P., & Kumar, S. P. (2011). Physical and biological response of the Arabian Sea to
921 tropical cyclone Phyan and its implications. *Marine Environmental Research*, *71*(5), 325-330.

922 Canadell, J.G., P.M.S. Monteiro, et al. 2021. Global Carbon and other Biogeochemical
923 Cycles and Feedbacks., in Climate Change 2021: The Physical Science Basis. Contribution of
924 Working Group I to the Sixth Assessment Report of the Intergovernmental Panel on Climate
925 Change, edited by L. G. Masson-Delmotte et al., Cambridge University Press.

926 Chakraborty, K., Valsala, V., Bhattacharya, T., & Ghosh, J. (2021). Seasonal cycle of surface
927 ocean pCO2 and pH in the northern Indian Ocean and their controlling factors. Progress in
928 Oceanography, 198, 102683.

929 Chakraborty, K., Kumar, N., Girishkumar, M. S., Gupta, G. V. M., Ghosh, J., Udaya
930 Bhaskar, T. V. S., & Thangaprakash, V. P. (2019). Assessment of the impact of spatial

resolution on ROMS simulated upper-ocean biogeochemistry of the Arabian Sea from an operational perspective. Journal of Operational Oceanography, 12(2), 116-142.

Chakraborty, K., Valsala, V., Gupta, G. V. M., & Sarma, V. V. S. S. (2018). Dominant biological control over upwelling on pCO2 in sea east of Sri Lanka. *Journal of Geophysical Research: Biogeosciences*, 123(10), 3250-3261.

Chandra, N., Patra, P. K., Niwa, Y., Ito, A., Iida, Y., Goto, D., et al. (2022). Estimated regional CO 2 flux and uncertainty based on an ensemble of atmospheric CO 2 inversions. *Atmospheric Chemistry and Physics*, *22*(14), 9215-9243.

Chau, T. T. T., Gehlen, M., & Chevallier, F. (2022). A seamless ensemble-based reconstruction of surface ocean pCO 2 and air–sea CO 2 fluxes over the global coastal and open oceans. *Biogeosciences*, 19(4), 1087-1109.

Chen, G., Wang, D., & Hou, Y., (2012). The features and interannual variability mechanism of mesoscale eddies in the Bay of Bengal. *Continental Shelf Research*. 47, 178–185.

Chevallier, F., Fisher, M., Peylin, P., Serrar, S., Bousquet, P., Bréon, F. M., et al. (2005). Inferring CO2 sources and sinks from satellite observations: Method and application to TOVS data. *Journal of Geophysical Research: Atmospheres*, *110*(D24).

Cocco, V., Joos, F., Steinacher, M., Frölicher, T. L., Bopp, L., Dunne, J., et al. (2013). Oxygen and indicators of stress for marine life in multi-model global warming projections. *Biogeosciences*, 10(3), 1849-1868.

Dalpadado, P., Arrigo, K. R., van Dijken, G. L., Gunasekara, S. S., Ostrowski, M., Bianchi, G., &Sperfeld, E. (2021). Warming of the Indian Ocean and its impact on temporal and spatial dynamics of primary production. *Progress in Oceanography*, *198*, 102688.

De Verneil, A., Lachkar, Z., Smith, S., & Lévy, M. (2022). Evaluating the Arabian Sea as a regional source of atmospheric CO 2: seasonal variability and drivers. *Biogeosciences*, 19(3), 907-929.

D'Mello, J. R., & Prasanna Kumar, S. (2018). Processes controlling the accelerated warming of the Arabian Sea. *International Journal of Climatology*, *38*(2), 1074-1086.

Davis, D., and Goyet, C. 2021. Balanced error sampling with applications to ocean biogeochemical sampling, University of Perpignan, France, pp. 214.

Dunstan, P. K., Foster, S. D., King, E., Risbey, J., O'Kane, T. J., Monselesan, D., et al. (2018). Global patterns of change and variation in sea surface temperature and chlorophyll a. *Scientific reports*, *8*(1), 1-9.

Fay, A. R., Gregor, L., Landschützer, P., McKinley, G. A., Gruber, N., Gehlen, M., et al. (2021). SeaFlux: harmonization of air–sea CO 2 fluxes from surface pCO 2 data products using a standardized approach. *Earth System Science Data*, *13*(10), 4693-4710.

Fay, A.R., McKinley, G.A., Lovenduski, N.S., Eddebbar, Y., Levy, M.N., Long, M.C., Olivarez, H.C., & Rustagi, R.R. (2023). Immediate and long-lasting impacts of the Mt. Pinatubo Eruption on Ocean oxygen and carbon inventories. Global Biogeochemical Cycles, 37, e2022GB007513.

Friedlingstein, P., Jones, M. W., O'Sullivan, M., Andrew, R. M., Bakker, D. C., Hauck, J., et al. (2022). Global carbon budget 2021. *Earth System Science Data*, *14*(4), 1917-2005.

George, M. D., Kumar, M. D., Naqvi, S. W. A., Banerjee, S., Narvekar, P. V., De Sousa, S. N., et al. (1994). A study of the carbon dioxide system in the northern Indian Ocean during premonsoon. *Marine Chemistry*, *47*(3-4), 243-254.

Ghosh, S., Sinha, P., Bhatla, R., Mall, R. K., & Sarkar, A. (2022). Assessment of Lead-Lag and Spatial Changes in simulating different epochs of the Indian summer monsoon using RegCM4. *Atmospheric Research*, *265*, 105892.

Ghosh, J., Chakraborty, K., Bhattacharya, T., Valsala, V., & Baduru, B. (2022). Impact of coastal upwelling dynamics on the pCO2 variability in the southeastern Arabian Sea. *Progress in Oceanography*, 203, 102785.

Gloege, L., Yan, M., Zheng, T., & McKinley, G. A. (2022). Improved quantification of ocean carbon uptake by using machine learning to merge global models and pCO2 data. *Journal of Advances in Modeling Earth Systems*, 14(2), e2021MS002620.

Goes, J. I., Tian, H., Gomes, H. D. R., Anderson, O. R., Al-Hashmi, K., deRada, S., et al. (2020). Ecosystem state change in the Arabian Sea fuelled by the recent loss of snow over the Himalayan-Tibetan plateau region. *Scientific reports*, *10*(1), 1-8.

Goyet, C., Millero, F. J., O'Sullivan, D. W., Eischeid, G., McCue, S. J., &Bellerby, R. G. J. (1998). Temporal variations of pCO2 in surface seawater of the Arabian Sea in 1995. *Deep Sea Research Part I: Oceanographic Research Papers*, *45*(4-5), 609-623.

Gregor, L., Lebehot, A. D., Kok, S., & Scheel Monteiro, P. M. (2019). A comparative assessment of the uncertainties of global surface ocean CO 2 estimates using a machine-learning ensemble (CSIR-ML6 version 2019a)–have we hit the wall?. *Geoscientific Model Development*, 12(12), 5113-5136.

Gregor, L., & Gruber, N. (2021). OceanSODA-ETHZ: a global gridded data set of the surface ocean carbonate system for seasonal to decadal studies of ocean acidification. *Earth System Science Data*, 13(2), 777-808.

Gruber, N., Gloor, M., Mikaloff Fletcher, S. E., Doney, S. C., Dutkiewicz, S., Follows, M. J., et al. (2009). Oceanic sources, sinks, and transport of atmospheric CO2. *Global biogeochemical cycles*, *23*(1).

Guglielmi V., F. Touratier, C.Goyet (2022a). Design of sampling strategy measurements of CO_2/carbonate properties. *Journal of Oceanography and Aquaculture*, 6(3): 000227. doi:10.23880/ijoac-16000227

Guglielmi V., F. Touratier, C. Goyet (2022b). Determination of discrete sampling locations minimizing both the number of samples and the maximum interpolation error: application to measurements of surface ocean properties. *Journal of Sea Research*, in revision

Iida, Y., Takatani, Y., Kojima, A., & Ishii, M. (2021). Global trends of ocean CO_2 sink and ocean acidification: an observation-based reconstruction of surface ocean inorganic carbon variables. *Journal of Oceanography*, 77(2), 323-358.

Jabaud-Jan, A., Metzl, N., Brunet, C., Poisson, A., &Schauer, B. (2004). Interannual variability of the carbon dioxide system in the southern Indian Ocean (20 S–60 S): The impact of a warm anomaly in austral summer 1998. *Global Biogeochemical Cycles*, *18*(1).

Körtzinger, A., Duinker, J. C., &Mintrop, L. (1997). Strong CO2 emissions from the Arabian Sea during south-west monsoon. *Geophysical Research Letters*, *24*(14), 1763-1766.

Kumar, M. D., Naqvi, S. W. A., George, M. D., & Jayakumar, D. A. (1996). A sink for atmospheric carbon dioxide in the northeast Indian Ocean. *Journal of Geophysical Research: Oceans*, *101*(C8), 18121-18125.

Kumari, V. R., Sarma, V. V. S. S., Mahesh, G., & Sudheer, A. K. (2022). Temporal variations in the chemical composition of aerosols over the coastal Bay of Bengal. *Atmospheric Pollution Research*, *13*(2), 101300.

Kumari, V.R., Sarma, V.V.S.S. & Dileep Kumar, M. (2022). Spatial variability in aerosol composition and its seawater acidification potential in coastal waters of the western coastal Bay of Bengal. *Journal of Earth System Science*, doi.org/10.1007/s12040-022-01996-w.

Kumari, V. R., Yadav, K., Sarma, V. V. S. S., & Dileep Kumar, M. (2021). Acidification of the coastal Bay of Bengal by aerosols deposition. *Journal of Earth System Science*, *130*(4), 1-13.

Kwiatkowski, L., Torres, O., Bopp, L., Aumont, O., Chamberlain, M., Christian, J. R., et al., (2020). Twenty-first century ocean warming, acidification, deoxygenation, and upper-ocean nutrient and primary production decline from CMIP6 model projections. *Biogeosciences*, 17(13), 3439-3470.

Lachkar, Z., Lévy, M., & Smith, S. (2018). Intensification and deepening of the Arabian Sea oxygen minimum zone in response to increase in Indian monsoon wind intensity. *Biogeosciences*, 15(1), 159-186.

Lachkar, Z., Mehari, M., Al Azhar, M., Lévy, M., & Smith, S. (2021). Fast local warming is the main driver of recent deoxygenation in the northern Arabian Sea. *Biogeosciences*, 18(20), 5831-5849.

Lachkar, Z., Smith, S., Lévy, M., &Pauluis, O. (2016). Eddies reduce denitrification and compress habitats in the Arabian Sea. *Geophysical Research Letters*, 43(17), 9148-9156.

Landschützer, P., Gruber, N., & Bakker, D. C. (2016). Decadal variations and trends of the global ocean carbon sink. *Global BiogeochemicalCycles*, 30(10), 1396-1417.

Lauvset, S. K., Gruber, N., Landschützer, P., Olsen, A., &Tjiputra, J. (2015). Trends and drivers in global surface ocean pH over the past 3 decades. *Biogeosciences*, *12*(5), 1285-1298.

Leseurre, C., Lo Monaco, C., Reverdin, G., Metzl, N., Fin, J., Mignon, C., & Benito, L. (2022). Summer trends and drivers of sea surface fCO_2 and pH changes observed in the southern Indian Ocean over the last two decades (1998–2019). *Biogeosciences*, *19*(10), 2599-2625.

Li, Y., Han, W., Hu, A., Meehl, G. A., & Wang, F. (2018). Multidecadal changes of the upper Indian Ocean heat content during 1965–2016. *Journal of Climate*, *31*(19), 7863-7884.

Landschützer, P., Gruber, N., & Bakker, D. C. (2016). Decadal variations and trends of the global ocean carbon sink. *Global Biogeochemical Cycles*, 30(10), 1396-1417.

Louanchi, F., Metzl, N., & Poisson, A. (1996). Modelling the monthly sea surface fCO2 fields in the Indian Ocean. *Marine Chemistry*, *55*(3-4), 265-279.

Lo Monaco, C. , Metzl, N., Fin, J., Mignon, C., Cuet, P., Douville, É., ... &Tribollet, A. (2021). Distribution and long-term change of the sea surface carbonate system in the Mozambique Channel (1963–2019). *Deep Sea Research Part II: Topical Studies in Oceanography*, 186, 104936.

McKinley, G. A., Fay, A. R., Eddebbar, Y. A., Gloege, L., &Lovenduski, N. S. (2020). External forcing explains recent decadal variability of the ocean carbon sink. *AGU Advances*, *1*(2), e2019AV000149.

Metzl, N. (2009). Decadal increase of oceanic carbon dioxide in Southern Indian Ocean surface waters (1991–2007). *Deep Sea Research Part II: Topical Studies in Oceanography*, *56*(8-10), 607-619.

Metzl, N., Beauverger, C., Brunet, C., Goyet, C., & Poisson, A. (1991). Surface water carbon dioxide in the southwest Indian sector of the Southern Ocean: a highly variable CO2 source/sink region in summer. *Marine Chemistry*, *35*(1-4), 85-95.

Metzl, N., Lo Monaco, C., Leseurre, C., Ridame, C., Fin, J., Mignon, C., et al. (2022). The impact of the South-East Madagascar Bloom on the oceanic CO 2 sink. *Biogeosciences*, *19*(5), 1451-1468.

Metzl, N., Louanchi, F., & Poisson, A. (1998). Seasonal and interannual variations of sea surface carbon dioxide in the subtropical Indian Ocean. *Marine Chemistry*, *60*(1-2), 131-146.

Metzl, N., Poisson, A., Louanchi, F., Brunet, C., Schauer, B., & Bres, B. (1995). Spatio-temporal distributions of air-sea fluxes of CO2 in the Indian and Antarctic Oceans: A first step. *Tellus B*, *47*(1-2), 56-69.

Millero, F. J., Degler, E. A., O'Sullivan, D. W., Goyet, C., &Eischeid, G. (1998). The carbon dioxide system in the Arabian Sea. *Deep Sea Research Part II: Topical Studies in Oceanography*, *45*(10-11), 2225-2252.

Miyama, T., Kominami, Y., Tamai, K., Nobuhiro, T., & Goto, Y. (2003). Automated foliage chamber method for long-term measurement of CO2 flux in the uppermost canopy. *Tellus B: Chemical and Physical Meteorology*, *55*(2), 322-330.

Mukhopadhyay, S. K., Biswas, H., De, T. K., Sen, S., & Jana, T. K. (2002). Seasonal effects on the air–water carbon dioxide exchange in the Hooghly estuary, NE coast of Bay of Bengal, India. *Journal of Environmental Monitoring*, *4*(4), 549-552.

Murtugudde, R., &Busalacchi, A. J. (1999). Interannual variability of the dynamics and thermodynamics of the tropical Indian Ocean. *Journal of Climate*, *12*(8), 2300-2326.

Murtugudde, R., McCreary Jr, J. P., &Busalacchi, A. J. (2000). Oceanic processes associated with anomalous events in the Indian Ocean with relevance to 1997–1998. *Journal of Geophysical Research: Oceans*, *105*(C2), 3295-3306.

Papa, F., Bala, S. K., Pandey, R. K., Durand, F., Gopalakrishna, V. V., Rahman, A., &Rossow, W. B. (2012). Ganga-Brahmaputra river discharge from Jason-2 radar altimetry: an update to the long-term satellite-derived estimates of continental freshwater forcing flux into the Bay of Bengal. *Journal of Geophysical Research: Oceans*, *117*(C11).

Pfeil, B., Olsen, A., Bakker, D. C., Hankin, S., Koyuk, H., Kozyr, A., et al. (2013). A uniform, quality controlled Surface Ocean CO 2 Atlas (SOCAT). *Earth System Science Data*, *5*(1), 125-143.

Poisson, A., Metzl, N., Brunet, C., Schauer, B., Bres, B., Ruiz-Pino, D., & Louanchi, F. (1993). Variability of sources and sinks of CO2 in the Western Indian and Southern Oceans during the year 1991. *Journal of Geophysical Research: Oceans*, *98*(C12), 22759-22778.

Rödenbeck, C., Bakker, D. C., Gruber, N., Iida, Y., Jacobson, A. R., Jones, S., et al. (2015). Data-based estimates of the ocean carbon sink variability–first results of the Surface Ocean pCO 2 Mapping intercomparison (SOCOM). *Biogeosciences*, *12*(23), 7251-7278.

1102 Rödenbeck, C., Keeling, R. F., Bakker, D. C., Metzl, N., Olsen, A., Sabine, C., & Heimann,
1103 M. (2013). Global surface-ocean p CO 2 and sea–air CO 2 flux variability from an
1104 observation-driven ocean mixed-layer scheme. *Ocean Science*, 9(2), 193-216.

1105 Roxy, M. K., Modi, A., Murtugudde, R., Valsala, V., Panickal, S., Prasanna Kumar, S., et al.
1106 (2016). A reduction in marine primary productivity driven by rapid warming over the tropical
1107 Indian Ocean. *Geophysical Research Letters*, *43*(2), 826-833.

1108 Roxy, M. K., Ritika, K., Terray, P., Murtugudde, R., Ashok, K., & Goswami, B. N. (2015).
1109 Drying of Indian subcontinent by rapid Indian Ocean warming and a weakening land-sea
1110 thermal gradient. *Nature communications*, *6*(1), 1-10.

1111 Sabine, C. L., Key, R. M., Johnson, K. M., Millero, F. J., Poisson, A., Sarmiento, J. L., et al.
1112 (1999). Anthropogenic CO2 inventory of the Indian Ocean. *Global Biogeochemical*
1113 *Cycles*, *13*(1), 179-198.

1114 Sabine, C. L., Wanninkhof, R., Key, R. M., Goyet, C., &Millero, F. J. (2000). Seasonal CO2
1115 fluxes in the tropical and subtropical Indian Ocean. *Marine Chemistry*, *72*(1), 33-53.

1116 Saji, N. H., Goswami, B. N., Vinayachandran, P. N., & Yamagata, T. (1999). A dipole mode
1117 in the tropical Indian Ocean. *Nature*, *401*(6751), 360-363.

1118 Sarma, V. V. S. S., Swathi, P. S., Kumar, M. D., Prasannakumar, S., Bhattathiri, P. M. A.,
1119 Madhupratap, M., et al. (2003). Carbon budget in the eastern and central Arabian Sea: An
1120 Indian JGOFS synthesis. *Global Biogeochemical Cycles*, *17*(4).

1121 Sarma, V. V. S. S. (2003). Monthly variability in surface pCO2 and net air-sea CO2 flux in
1122 the Arabian Sea. *Journal of Geophysical Research: Oceans*, *108*(C8).

1123 Sarma, V. V. S. S. (2006). The influence of Indian Ocean Dipole (IOD) on biogeochemistry
1124 of carbon in the Arabian Sea during 1997–1998. *Journal of earth system science*, *115*(4),
1125 433-450.

1126 Sarma, V. V. S. S., Krishna, M. S., & Srinivas, T. N. R. (2020). Sources of organic matter
1127 and tracing of nutrient pollution in the coastal Bay of Bengal. *Marine Pollution Bulletin*, *159*,
1128 111477.

1129 Sarma, V. V. S. S., Krishna, M. S., Paul, Y. S., &Murty, V. S. N. (2015). Observed changes
1130 in ocean acidity and carbon dioxide exchange in the coastal Bay of Bengal–a link to air
1131 pollution. *Tellus B: Chemical and Physical Meteorology*, *67*(1), 24638.

1132 Sarma, V. V. S. S., Krishna, M. S., Rao, V. D., Viswanadham, R., Kumar, N. A., Kumari, T.
1133 R., et al. (2012). Sources and sinks of CO2 in the west coast of Bay of Bengal. *Tellus B:*
1134 *Chemical and Physical Meteorology*, *64*(1), 10961.

1135 Sarma, V. V. S. S., Krishna, M. S., Srinivas, T. N. R., Kumari, V. R., Yadav, K., & Kumar,
1136 M. D. (2021). Elevated acidification rates due to deposition of atmospheric pollutants in the
1137 coastal Bay of Bengal. *Geophysical Research Letters*, *48*(16), e2021GL095159.

1138 Sarma, V. V. S. S., Kumar, G. S., Yadav, K., Dalabehera, H. B., Rao, D. N., Behera, S., &
1139 Loganathan, J. (2019). Impact of eddies on dissolved inorganic carbon components in the
1140 Bay of Bengal. *Deep Sea Research Part I: Oceanographic Research Papers*, *147*, 111-120.

1141 Sarma, V. V. S. S., Kumar, M. D., & George, M. D. (1998). The central and eastern Arabian
1142 Sea as a perennial source of atmospheric carbon dioxide. *Tellus B: Chemical and Physical*
1143 *Meteorology*, *50*(2), 179-184.

Sarma, V. V. S. S., Kumar, M. D., Gauns, M., &Madhupratap, M. (2000). Seasonal controls on surface pCO2 in the central and eastern Arabian Sea. *Journal of Earth System Science*, 109(4), 471-479.

Sarma, V. V. S. S., Kumar, M. D., George, M. D., & Rajendran, A. (1996). Seasonal variations in inorganic carbon components in the central and eastern Arabian Sea. *Current Science*, 852-856.

Sarma, V. V. S. S., Kumari, V. R., Srinivas, T. N. R., Krishna, M. S., Ganapathi, P., &Murty, V. S. N. (2018). East India Coastal Current controls the dissolved inorganic carbon in the coastal Bay of Bengal. *Marine Chemistry*, *205*, 37-47.

Sarma, V. V. S. S., Lenton, A., Law, R. M., Metzl, N., Patra, P. K., Doney, S., et al. (2013). Sea–air CO 2 fluxes in the Indian Ocean between 1990 and 2009. *Biogeosciences*, 10(11), 7035-7052.

Sarma, V. V. S. S., Prasad, M. H. K., &Dalabehera, H. B. (2021). Influence of phytoplankton pigment composition and primary production on pCO2 levels in the Indian Ocean. *Journal of Earth System Science*, *130*(2), 1-16.

Sarma, V. V. S. S., Rao, G. D., Viswanadham, R., Sherin, C. K., Salisbury, J., Omand, M. M., et al. (2016). Effects of freshwater stratification on nutrients, dissolved oxygen, and phytoplankton in the Bay of Bengal. *Oceanography*, *29*(2), 222-231.

Schott, F. A., & McCreary Jr, J. P. (2001). The monsoon circulation of the Indian Ocean. *Progress in Oceanography*, *51*(1), 1-123.

Schott, F. A., Dengler, M., &Schoenefeldt, R. (2002). The shallow overturning circulation of the Indian Ocean. *Progress in oceanography*, *53*(1), 57-103.

Schott, F. A., Xie, S. P., & McCreary Jr, J. P. (2009). Indian Ocean circulation and climate variability. *Reviews of Geophysics*, *47*(1).

Sridevi, B., &Sarma, V. V. S. S. (2021). Role of river discharge and warming on ocean acidification and pCO2 levels in the Bay of Bengal. *Tellus B: Chemical and Physical Meteorology*, *73*(1), 1-20.

Sridevi, B, Sabira, Sk., & Sarma, V.V.S.S. (2023). Impact of ocean warming on net primary production in the northern Indian Ocean: role of aerosols and freshening of surface ocean. Environmental Science and Pollution Research, doi: 10.1007/s11356-023-26001-9.

Sutton, A. J., Feely, R. A., Maenner-Jones, S., Musielwicz, S., Osborne, J., Dietrich, C., Monacci, N., Cross, J., Bott, R., Kozyr, A., Andersson, A. J., Bates, N. R., Cai, W.-J., Cronin, M. F., De Carlo, E. H., Hales, B., Howden, S. D., Lee, C. M., Manzello, D. P., McPhaden, M. J., Meléndez, M., Mickett, J. B., Newton, J. A., Noakes, S. E., Noh, J. H., Olafsdottir, S. R., Salisbury, J. E., Send, U., Trull, T. W., Vandemark, D. C., and Weller, R. A. (2019) Autonomous seawater pCO_2 and pH time series from 40 surface buoys and the emergence of anthropogenic trends, Earth Syst. Sci. Data, 11, 421-439, https://doi.org/10.5194/essd-11-421-2019.

Swapna, P., Sreeraj, P., Sandeep, N., Jyoti, J., Krishnan, R., Prajeesh, A. G., et al. (2022). Increasing frequency of extremely severe cyclonic storms in the north Indian Ocean by anthropogenic warming and southwest monsoon weakening. *Geophysical Research Letters*, 49(3), e2021GL094650.

Takahashi, T., Sutherland, S. C., Wanninkhof, R., Sweeney, C., Feely, R. A., Chipman, D. W., et al. (2009). Climatological mean and decadal change in surface ocean pCO2, and net

sea–air CO2 flux over the global oceans. *Deep Sea Research Part II: Topical Studies in Oceanography*, *56*(8-10), 554-577.

Thompson, D. W., & Solomon, S. (2002). Interpretation of recent Southern Hemisphere climate change. *Science*, *296*(5569), 895-899.

Valsala, V., &Maksyutov, S. (2013). Interannual variability of the air–sea CO2 flux in the north Indian Ocean. *Ocean Dynamics*, *63*(2), 165-178.

Valsala, V., Sreeush, M. G., & Chakraborty, K. (2020). The IOD impacts on the Indian Ocean Carbon cycle. *Journal of Geophysical Research: Oceans*, *125*(11), e2020JC016485.

Valsala, V., Sreeush, M. G., Anju, M., Sreenivas, P., Tiwari, Y. K., Chakraborty, K., & Sijikumar, S. (2021). An observing system simulation experiment for Indian Ocean surface pCO2 measurements. *Progress in Oceanography*, *194*, 102570.

Wanninkhof, R. (1992). Relationship between wind speed and gas exchange over the ocean. *Journal of Geophysical Research: Oceans*, *97*(C5), 7373-7382.

Wanninkhof, R. (2014). Relationship between wind speed and gas exchange over the ocean revisited. *Limnology and Oceanography: Methods*, *12*(6), 351-362.

Watson, A. J., Schuster, U., Shutler, J. D., Holding, T., Ashton, I. G., Landschützer, P., et al. (2020). Revised estimates of ocean-atmosphere CO2 flux are consistent with ocean carbon inventory. *Nature communications*, 11(1), 1-6.

Xie, S. P., Annamalai, H., Schott, F. A., & McCreary Jr, J. P. (2002). Structure and mechanisms of South Indian Ocean climate variability. *Journal of Climate*, *15*(8), 864-878.

Yadav, K., Rao, V. D., Sridevi, B., &Sarma, V. V. S. S. (2021). Decadal variations in natural and anthropogenic aerosol optical depth over the Bay of Bengal: the influence of pollutants from Indo-GangeticPlain. *Environmental Science and Pollution Research*, *28*(39), 55202-55219.

Ye, H., Sheng, J., Tang, D., Morozov, E., Kalhoro, M. A., Wang, S., & Xu, H. (2019). Examining the Impact of Tropical Cyclones on Air-Sea CO2 Exchanges in the Bay of Bengal Based on Satellite Data and In Situ Observations. *Journal of Geophysical Research: Oceans*, *124*(1), 555-576.

Zhang, J., & Reid, J. S. (2010). A decadal regional and global trend analysis of the aerosol optical depth using a data-assimilation grade over-water MODIS and Level 2 MISR aerosol products. *Atmospheric Chemistry and Physics*, *10*(22), 10949-10963.

Zeng, J., Nojiri, Y., Landschützer, P., Telszewski, M., & Nakaoka, S. I. (2014). A global surface ocean f CO 2 climatology based on a feed-forward neural network. *Journal of Atmospheric and Oceanic Technology*, 31(8), 1838-1849.

Table 1: Details of the hindcast models (including regional models) with reference to a period of the run, products used, parameterization of transfer velocity and resolution of the model.

Global hindcast model	Period for Analysis	Spun-up	Initial conditions/physical forcing	wind	Riverine input used	Transfer velocity	resolution
CCSM-WHOI	1958-2017						1^0 x 1^0
CESM-ETHZ	1980-2018	Spun-up to preindustrial steady state with 287.4 ppm	POP2 model was initialized with Levitus data and state of rest Does not include the phosphoric and silicic acid systems	JRA	No	Wanninkhof 1992	~1^0 x1.125^0
CNRM-ESM2-1	1980-2018	Preindustrial; 1850 global average CO2 set to 286.46 ppm	Physical: NCEP-2; air-sea flux data: CORE II; atm.CO2: **GCP** Global averaged annual CO2 Includes the phosphoric and silicic acid systems		Yes	Wanninkhof 2014	1^0 x 1^0
EC-Earth3	1980-2018	Preindustrial steady state 284.32 ppm for 1850	O2, Nutrients: WOA13 DIC, Alkalinity: GLODAPv2; Freshwater input: OMIP2 from JRA1.4-55	JRA55	Yes	Wanninkhof 1992	1x 1^0
FESOM_REcoM_LR (FESOM-1.4-REcoM2-LR	1981-2019	Physical spun-up on HR mesh 1 with constant atm. CO2 BGC fields on LR mesh of 1980 year 278 ppm	atm.CO2: **GCP** Global averaged annual CO2 O2, Nutrients: WOA13 DIC, Alkalinity: GLODAPv2	JRA55	No	Wanninkhof 2014	1^0 x 1^0
MOM6-Princeton	1980-2018	Atm. CO2 for preindustrial steady state: 278 ppm, Spun-up starting from 1959,	SST, SSS, nutrients: WOA13; DIC & Alkalinity: GLODAPv2; does not include Phosphoric and silicic acid systems. Alkalinity is influenced by inputs from river, calcium carbonate burial to the sediment and nitrogen redox change	JRA	Yes	Wanninkhof 1992	0.5^0 x 0.5^0
MPIOM-HAMOCC	1980-2019	Preindustrial steady state 296.2 ppm atm.CO2	Atmospheric CO2 concentrations are according to the link provided in the RECCAP2 protocol Included phosphoric and silicic acid systems	NCEP	No	Wanninkhof 1992 & 2014	Bipolar grid with 1.5^0 near equator
MRI-ESM2-1	1980-2018	Preindustrial steady state 284.32 ppm	Initialized with those derived from GLODAPv2 and WOA13v2. SST, SSS, nutrients: WOA13v2	JRA 55	No	Wanninkhof 1992 & 2014	Nominally 100 km
NorESM-OC1.2	1980-2018	Preindustrial steady state	Nutrients: WOA13;		No	Wanninkhof 1992	Nominal 1^0

		for 1000 years CO2 set to 278 ppm	DIC and Alkalinity: GLODAPv2 Included phosphoric and silicic acid systems				
ORCA1_LIM3-PISCES (IPSL-NEMO-PISCES)	1980-2018	Initialized with observations in year 1836 and CO2 set to 286.46 ppm at 1870 level	DIC & Alkalinity GLODAPv2 Included phosphoric and silicic acid systems	JRA55	Yes	Wanninkhof 1992	1^0 x 1^0
ORCA025-GEOMAR	1980-2018	Preindustrial steady state for 137 years and CO2 set to 284.32 ppm	Levitus 1998; (SST & SSS) Nutrients: WOAv2 DIC &Alk: GLODAP Pre-spin-up for sea ice from different experiments	JRA55	No	Wanninkhof 1992	$1/4^0$
Planktom12	1980-2018	Spun-up to 1750-1947 with looped 1990 NCEP forcing; Preindustrial steady state 278 ppm	NCEP forcing Sea-ice: NEMO-LIM2 model Included phosphoric and silicic acid systems			Wanninkhof 1992	1^0 x 1^0
Regional hindcast models							
INCOIS-BIO-ROMS	1980-2018	Initialized with observations for a particular year (1970) RECCAP2 Strategy 1	Atm.CO2: Keeling et.al., 1995 at monthly resolution. The physical state variables have been initialized using ECDA system simulated reanalysis data produced by GFDL. The biological state variables (NO3, Chlorophyll-a, O2, etc.) have been initialized using the climatological state of January generated from the climatological run of the model. The model state of the carbon state variables has been initialized using the Global Ocean Data Product (GLODAP; Key et al., 2004).	JRA55-do	Yes	Wanninkhof 2014	$1/12^0$
ROMS-NYUAD	1980-2018	1950-1979 (repeated normal year for physical forcing, increasing pCO2 from Joos and Spahni (2008) and Keeling et al. (2005).	temp, salinity, u, v, SSH: ORAS5; O2 & nitrate: WOA18 Chl-a: CMEMS (SeaWiFS& MODIS) DIC &Alk, GLODAPv2	ERA-Interim	Yes	Wanninkhof 1992	0.1 x 0.1

1225

Table 2: The methods used in the different observation-based surface CO_2 models used in this study.

Observation-based surface CO_2 models	**Method**	**Reference**
CMEMS-LSCE-FFNN	Feed Forward Neural Network (FFNN)	Chau et al., 2022
CSIRML6	Machine Learning/CSIR-ML6	Gregor et al., 2019
Jena-MLS (CarboScope)	/ocean mixed layer model	Rodenbeck et al., 2013
JMAMLR	Multiple Linear Regression model	Iida et al., 2021
Spco2_LDEO HPD	Global Ocean Biogeochem Model/Extreme Gradient Boosting (XGB)	Gloege et al., 2022
SOMFNN	Neural Network	Landschutzer et al., 2016
NIES-MLR3	Feed Forward Neural Network (FFNN)	Zeng et al., 2014
OceanSODAETHZ	Geospatial Random Cluster Emsemble Regression (GRaCER)	Gregor and Gruber 2021
UOEX_WAT20	Multiple Linear Regression/ Feed Forward Neural Network (FFNN)	Watson et al., 2020

Table 3: The annual mean uptake (±standard deviation) of CO_2 from the climatology (Takahahi et al, 2009), hindcast, empirical and atmospheric inversion models. All units in PgC yr^{-1}. The negative values represent CO_2 flux into the ocean and the positive ones into the atmosphere.

Region	Climatology	Hindcast Models (Includes 2 Regional models) (n=14)	Observation-based models (n=9)	Atmospheric Inversion models (n=2)	All models (n=25)	Surface area (km^2)
Arabian Sea	0.08 ± 0.06	0.03 ± 0.01	0.08 ± 0.01	0.16 ± 0.12	0.06 ± 0.05	0.70×10^7
Bay of Bengal	0.01 ± 0.01	-0.00 ± 0.01	0.01 ± 0.00	0.01 ± 0.01	0.00 ± 0.01	0.44×10^7
Equatorial Indian Ocean	0.04 ± 0.03	-0.05 ± 0.04	0.02 ± 0.02	0.02 ± 0.03	-0.02 ± 0.05	1.55×10^7
South Indian Ocean	-0.20 ± 0.16	-0.19 ± 0.06	-0.23 ± 0.02	-0.46 ± 0.30	-0.23 ± 0.11	1.24×10^7
Indian Ocean	-0.07 ± 0.14	-0.21 ± 0.10	-0.13 ± 0.04	-0.27 ± 0.16	-0.19 ± 0.10	3.92×10^7

Table 4: The growth rate (±standard deviation) of pCO_2 (µatm yr^{-1}) in the different regions of the Indian Ocean and different periods. The p-value of the regression of time-series pCO_2 variability is given in bracket.

Period	Arabian Sea		Bay of Bengal		Equatorial Indian Ocean		South Indian Ocean		Indian Ocean	
(µatm/yr)	hindcast	Empirical	hindcast	Empirical	hindcast	Empirical	hindcast	Empirical	hindcast	Empirical
1985-2018	1.68±0.03 (7.7E-32)	1.64±0.02 (1.8E-39)	1.54±0.04 (5.4E-28)	1.64±0.02 (7.2E-38)	1.72±0.03 (1.1E-31)	1.65±0.02 (1.3E-38)	1.73±0.03 (1.8E-32)	1.70±0.02 (2.6E-37)	1.70±0.03 (4.6E-33)	1.67±0.02 (4.7E-39)
1985-2000	1.32±0.07 (3.7E-11)	1.41±0.04 (3.3E-15)	1.34±0.15 (5.2E-07)	1.46±0.05 (1.4E-13)	1.43±0.09 (1.6E-10)	1.52±0.04 (5.00E-15)	1.43±0.08 (6.9E-11)	1.50±0.05 (4.6E-14)	1.41±0.08 (2.9E-11)	1.49±0.04 (1.6E-15)
2001-2018	1.88±0.06 (2.1E-15)	1.76±0.03 (9.6E-21)	1.71±0.06 (1.6E-14)	1.76±0.05 (4.7E-17)	2.01±0.05 (5.2E-17)	1.82±0.04 (1.30E-17)	1.98±0.05 (9.4E-17)	1.91±0.03 (8.1E-21)	1.96±0.04 (3.9E-18)	1.84±0.03 (9.3E-20)

Table 5: Rate of changes in CO_2 fluxes (±standard deviation) (PgC yr^{-1} $decade^{-1}$) in the Indian Ocean during different time periods. The p-value of the regression of time-series CO_2 variability is given in bracket. The negative values represent the decrease in source and vice versa for the positive.

Period	Arabian Sea		Bay of Bengal		Equatorial Indian Ocean		South Indian Ocean		Indian Ocean	
	hindcast	**Empirical**	**hindcast**	**Empirical**	**hindcast**	**Empirical**	**hindcast**	**Empirical**	**hindcast**	**Empirical**
1985-2018	-0.003±0.001 (3.5E-05)	-0.006±0.001 (2.7E-09)	-0.004±0.000 (2.4E-09)	-0.002±0.0001 (3.14E-05)	-0.007±0.001 (7.3E-06)	-0.006±0.002 (6.0E-04)	-0.010±0.002 (1.9E-05)	-0.008±0.002 (1.8E-05)	-0.023±0.003 (1.4E-08)	-0.021±0.003 (1.2E-07)
1985-2000	-0.001±0.002 (5.4E-01)	-0.002±0.002 (4.7E-01)	-0.002±0.002 (2.4E-01)	0.001±0.001 (2.3E-01)	-0.004±0.005 (3.7E-01)	0.010±0.003 (4.2E-03)	-0.020±0.006 (4.2E-03)	-0.003±0.005 (5.0E-01)	-0.028±0.012 (3.2E-02)	0.007±0.007 (3.7E-01)
2001-2018	-0.005±0.002 (7.8E-03)	-0.011±0.001 (1.8E-07)	-0.005±0.001 (3.0E-06)	-0.005±0.0001 (8.5E-09)	-0.006±0.003 (8.1E-02)	-0.018±0.002 (1.1E-07)	-0.006±0.005 (2.0E-01)	-0.012±0.004 (9.1E-03)	-0.023±0.007 (4.0E-03)	-0.046±0.005 (6.2E-08)

Figure 1: a) Figure showing the sub-regions of the Indian Ocean used in this study: South Indian Ocean (SIO; Brown), equatorial Indian Ocean (EIO; red), Arabian Sea (AS; Blue) and Bay of Bengal (BoB; green). b) shows the location of observations of oceanic pCO2 collected since 1958 (Bakker et al., 2020), c) CO_2 flux climatology based on the observations and interpolated to a 4 x 5^{o} grid (Takahashi et al., 2009) and d) Annual mean uptake from climatology, hindcast, empirical and atmospheric inversions models (PgC yr^{-1}) for the reference year of 2002. The error bars represent the standard deviation. The negative values represent fluxes into the ocean and positive to the atmosphere.

Figure 2: Annual mean uptake (in mol m^{-2} yr^{-1}) from the 14 hindcasts (2 regional) models for the reference year of 2002. The negative values reflect fluxes into the ocean and are positive for the atmosphere.

Figure 3: Annual mean uptake (in mol m^{-2} yr^{-1}) from the 9 observation-based models for the reference year of 2002. The negative values reflect fluxes into the ocean and are positive for the atmosphere.

Figure 4: Annual mean uptake (in mol m^{-2} yr^{-1}) from the 2 atmospheric inversion models. The CAMSv20r1 used inter-annually varying prior fluxes from an empirical model CEMES, while MACTM used annually repeating prior flux seasonality from Takahashi et al. (2009). The negative values reflect fluxes into the ocean and are positive for the atmosphere.

Figure 5: The zonally integrated, annual mean CO_2 uptake (30^{o}N-37.5^{o}S) from a) hindcast, b) empirical and c) atmospheric inversion models.

Figure 6: Seasonal cycle of the CO_2 fluxes (PgC yr^{-1}; left panel) and δpCO_2 (µatm; right panel) in the Indian Ocean from observations, mean hindcast, empirical and atmospheric inversion models in the Indian Ocean, Arabian Sea, BoB, EIO and SIO.

Figure 7: The inter-annual variability from hindcast, empirical and atmospheric inversion models. The upper panel shows the ENSO (https://ggweather.com/enso/oni.htm) and IOD index (http://www.bom.gov.au/climate/iod/) and the other panels for the entire Indian Ocean, Arabian Sea, Bay of Bengal, equatorial Indian Ocean, and South Indian Ocean. The trends of mean hindcast, empirical and atmospheric inversion are given in PgC yr^{-1} decade^{-1}.

Figure 1.

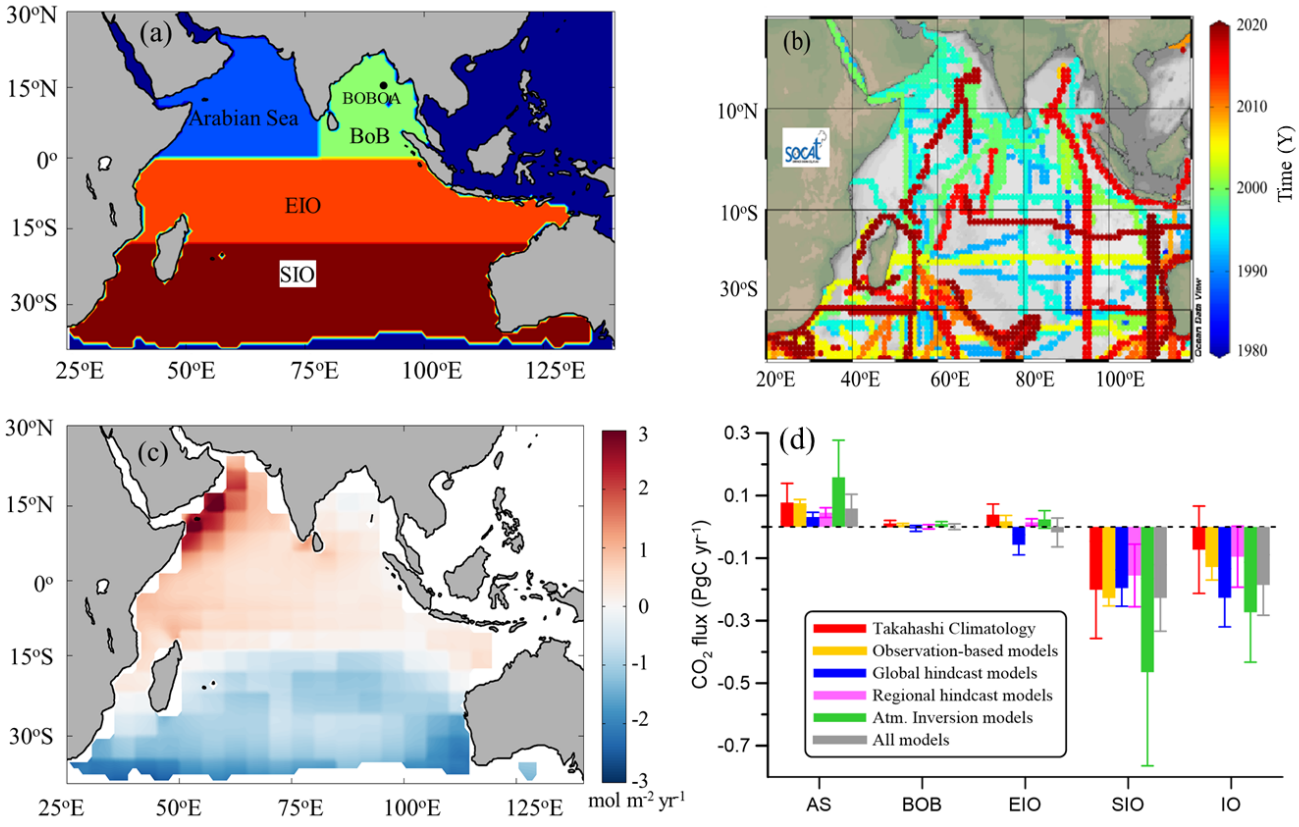
(a)
Arabian Sea
BOBOA
BoB
EIO
SIO
30°N
15°N
0°
15°S
30°S
25°E
50°E
75°E
100°E
125°E
(b)
10°N
10°S
30°S
20°E
40°E
60°E
80°E
100°E
2020
2010
2000
1990
1980
Time (Y)
(c)
3
2
1
0
-1
-2
-3
mol m-2 yr-1
(d)
0.3
0.1
-0.1
-0.3
-0.5
-0.7
CO2 flux (PgC yr-1)
Takahashi Climatology
Observation-based models
Global hindcast models
Regional hindcast models
Atm. Inversion models
All models
AS
BOB
EIO
SIO
IO

Figure 2.

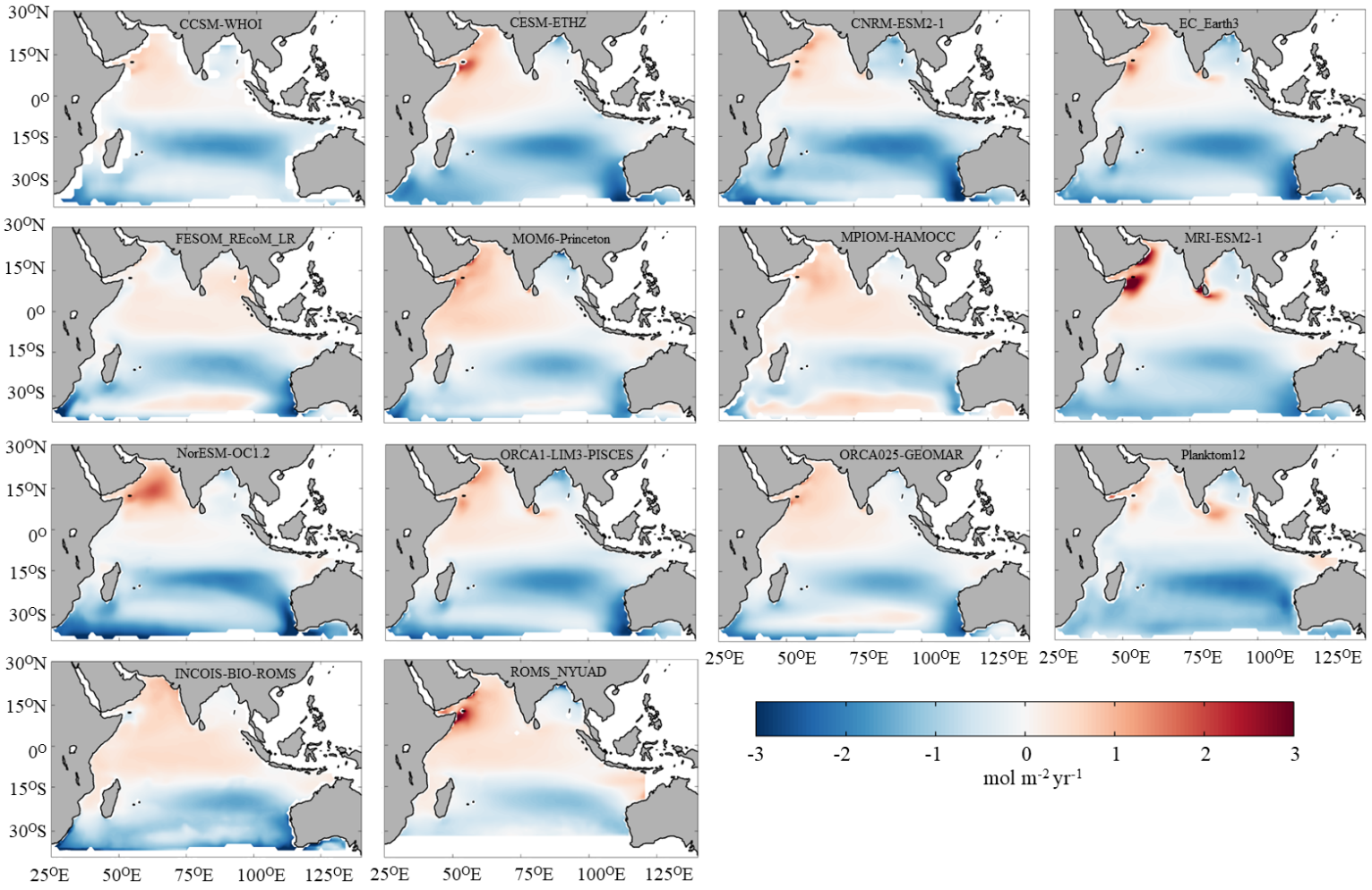
CCSM-WHOI
CESM-ETHZ
CNRM-ESM2-1
EC_Earth3
FESOM_REcoM_LR
MOM6-Princeton
MPIOM-HAMOCC
MRI-ESM2-1
NorESM-OC1.2
ORCA1-LIM3-PISCES
ORCA025-GEOMAR
Planktom12
INCOIS-BIO-ROMS
ROMS_NYUAD
30°N
15°N
0°
15°S
30°S
25°E
50°E
75°E
100°E
125°E
-3
-2
-1
0
1
2
3
mol m-2 yr-1

Figure 3.

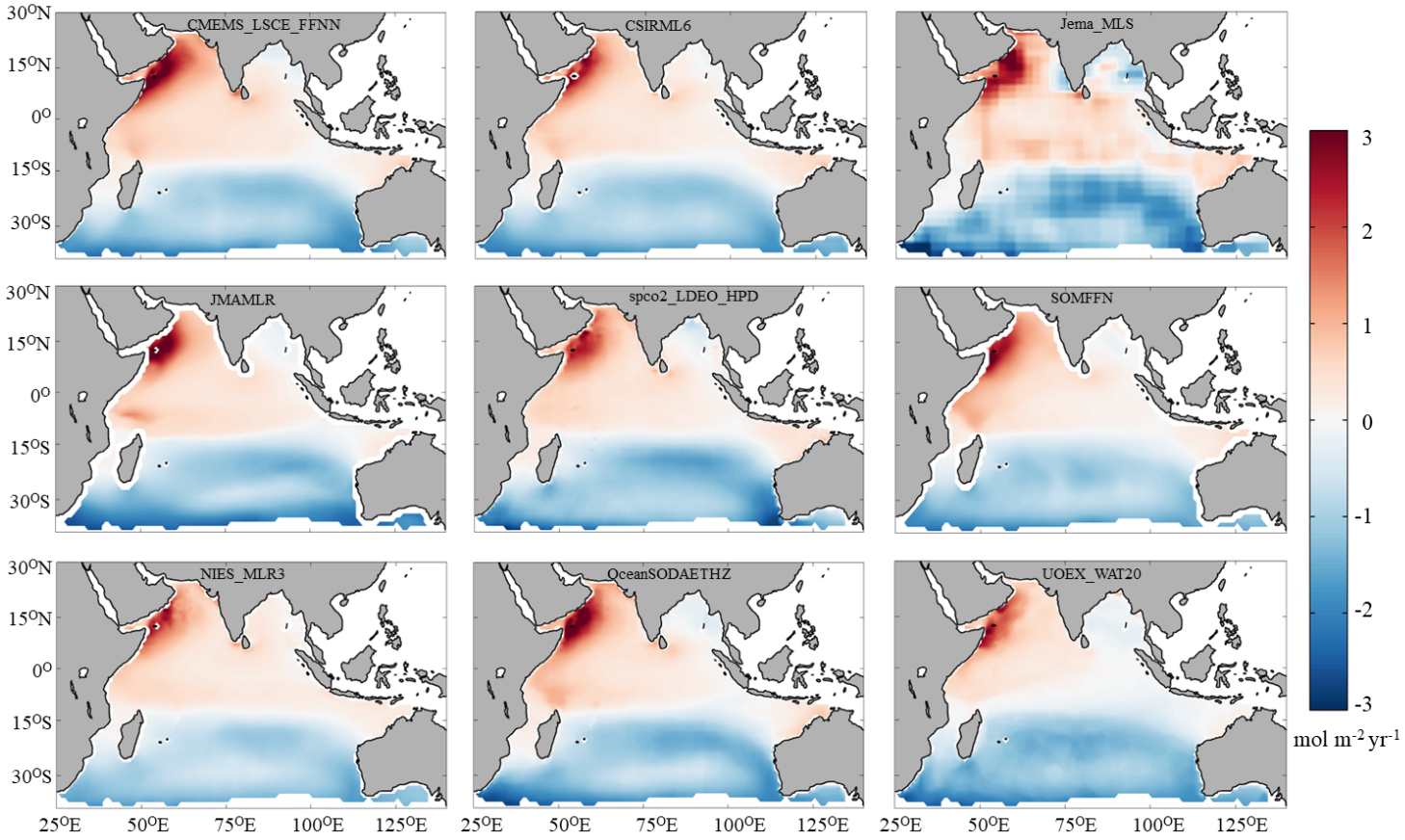
CMEMS_LSCE_FFNN
CSIRML6
Jema_MLS
JMAMLR
spco2_LDEO_HPD
SOMFFN
NIES_MLR3
OceanSODAETHZ
UOEX_WAT20
30°N
15°N
0°
15°S
30°S
25°E
50°E
75°E
100°E
125°E
3
2
1
0
-1
-2
-3
mol m-2 yr-1

Figure 4.

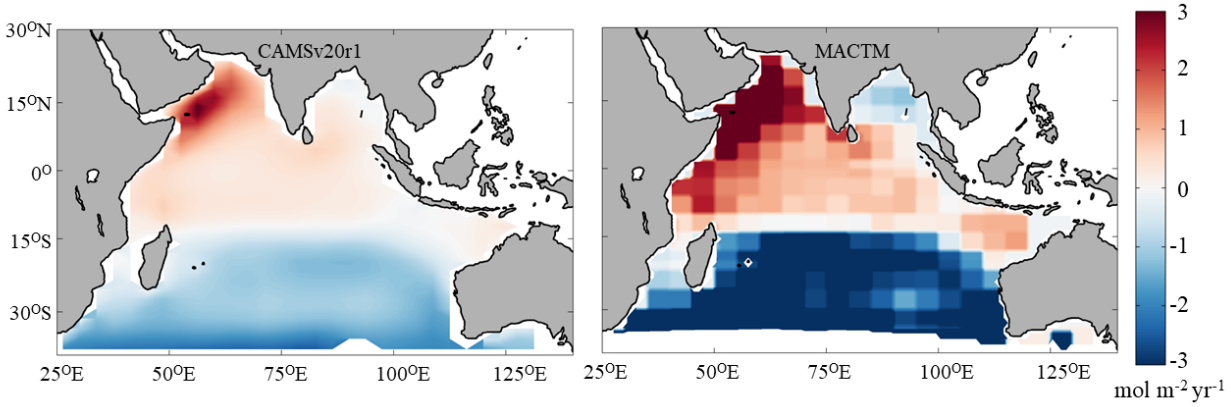
CAMSv20r1
MACTM
30°N
15°N
0°
15°S
30°S
25°E
50°E
75°E
100°E
125°E
3
2
1
0
-1
-2
-3
mol m-2 yr-1

Figure 5.

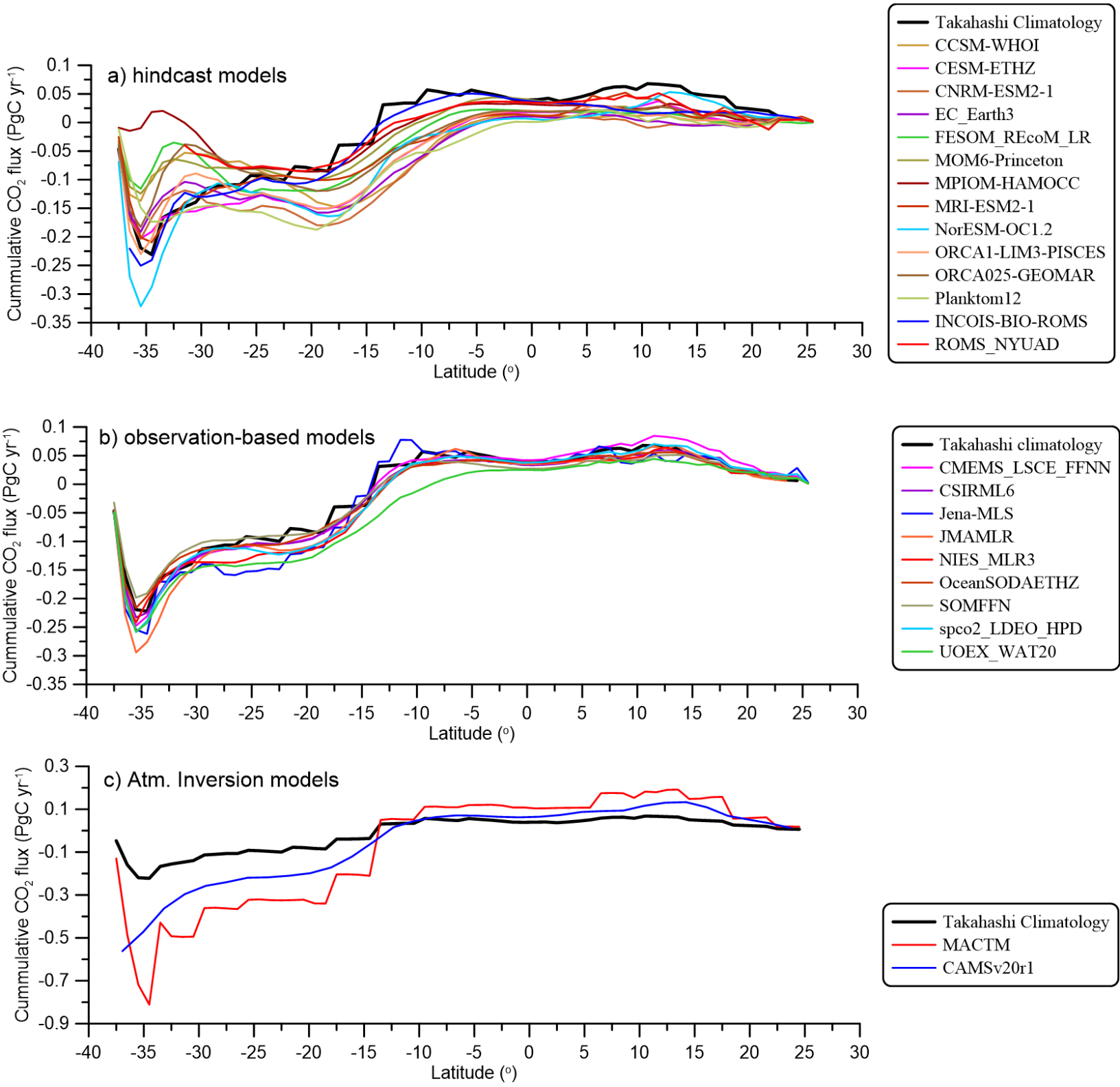
a) hindcast models
Cummulative CO2 flux (PgC yr-1)
Latitude (°)
Takahashi Climatology
CCSM-WHOI
CESM-ETHZ
CNRM-ESM2-1
EC_Earth3
FESOM_REcoM_LR
MOM6-Princeton
MPIOM-HAMOCC
MRI-ESM2-1
NorESM-OC1.2
ORCA1-LIM3-PISCES
ORCA025-GEOMAR
Planktom12
INCOIS-BIO-ROMS
ROMS_NYUAD
b) observation-based models
Cummulative CO2 flux (PgC yr-1)
Latitude (°)
Takahashi climatology
CMEMS_LSCE_FFNN
CSIRML6
Jena-MLS
JMAMLR
NIES_MLR3
OceanSODAETHZ
SOMFFN
spco2_LDEO_HPD
UOEX_WAT20
c) Atm. Inversion models
Cummulative CO2 flux (PgC yr-1)
Latitude (°)
Takahashi Climatology
MACTM
CAMSv20r1

Figure 6.

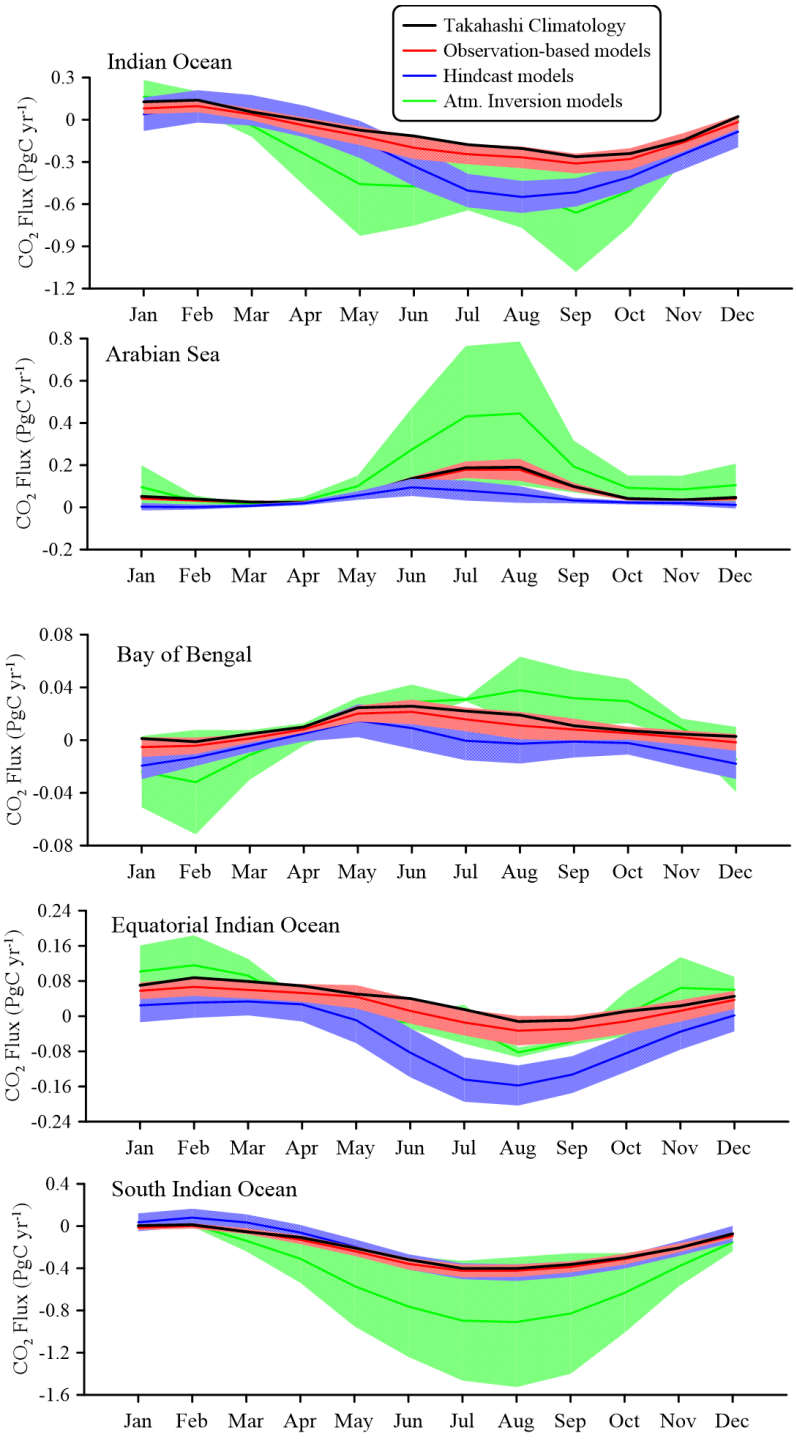
Takahashi Climatology
Observation-based models
Hindcast models
Atm. Inversion models
Indian Ocean
Arabian Sea
Bay of Bengal
Equatorial Indian Ocean
South Indian Ocean
CO2 Flux (PgC yr-1)
Jan Feb Mar Apr May Jun Jul Aug Sep Oct Nov Dec

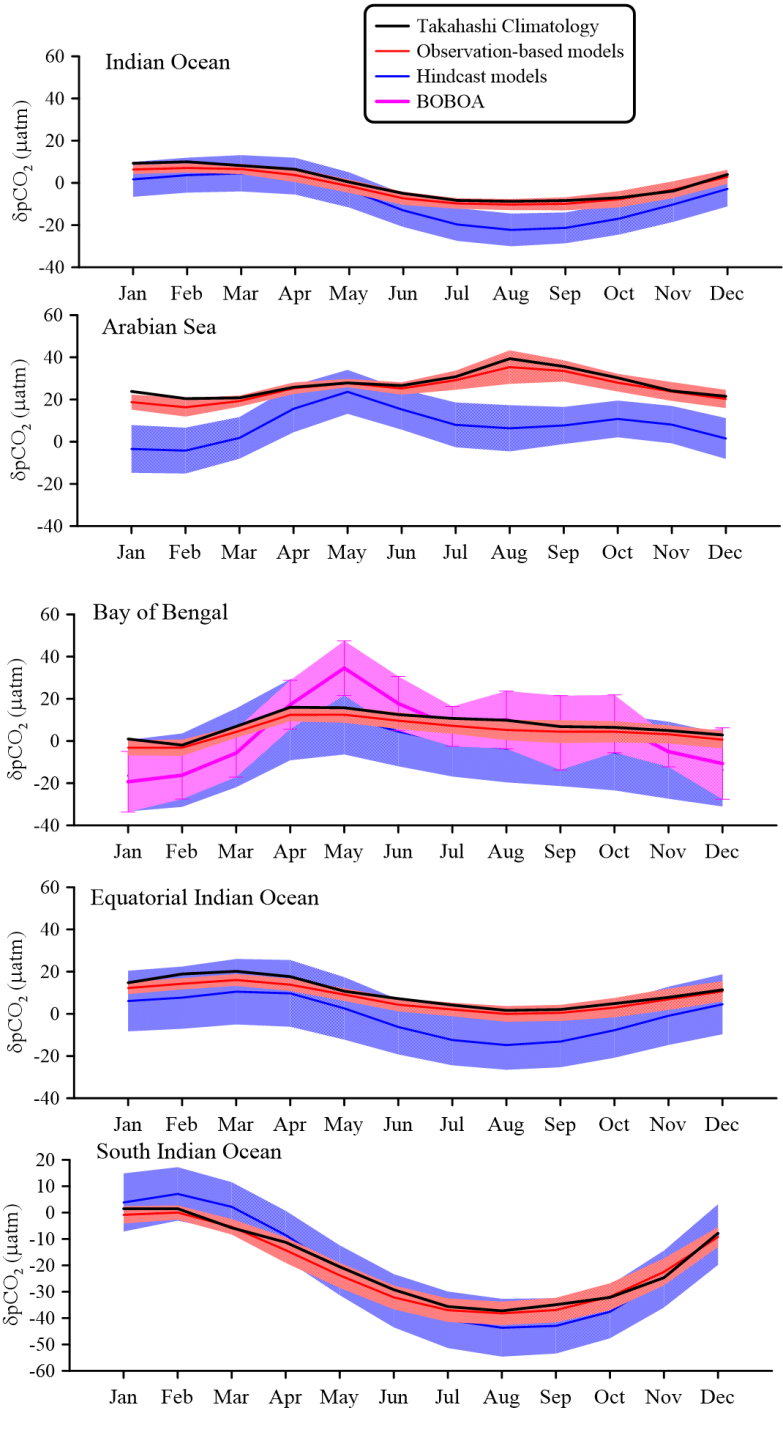
Takahashi Climatology
Observation-based models
Hindcast models
BOBOA
Indian Ocean
Arabian Sea
Bay of Bengal
Equatorial Indian Ocean
South Indian Ocean
δpCO2 (µatm)
Jan Feb Mar Apr May Jun Jul Aug Sep Oct Nov Dec

Figure 7.

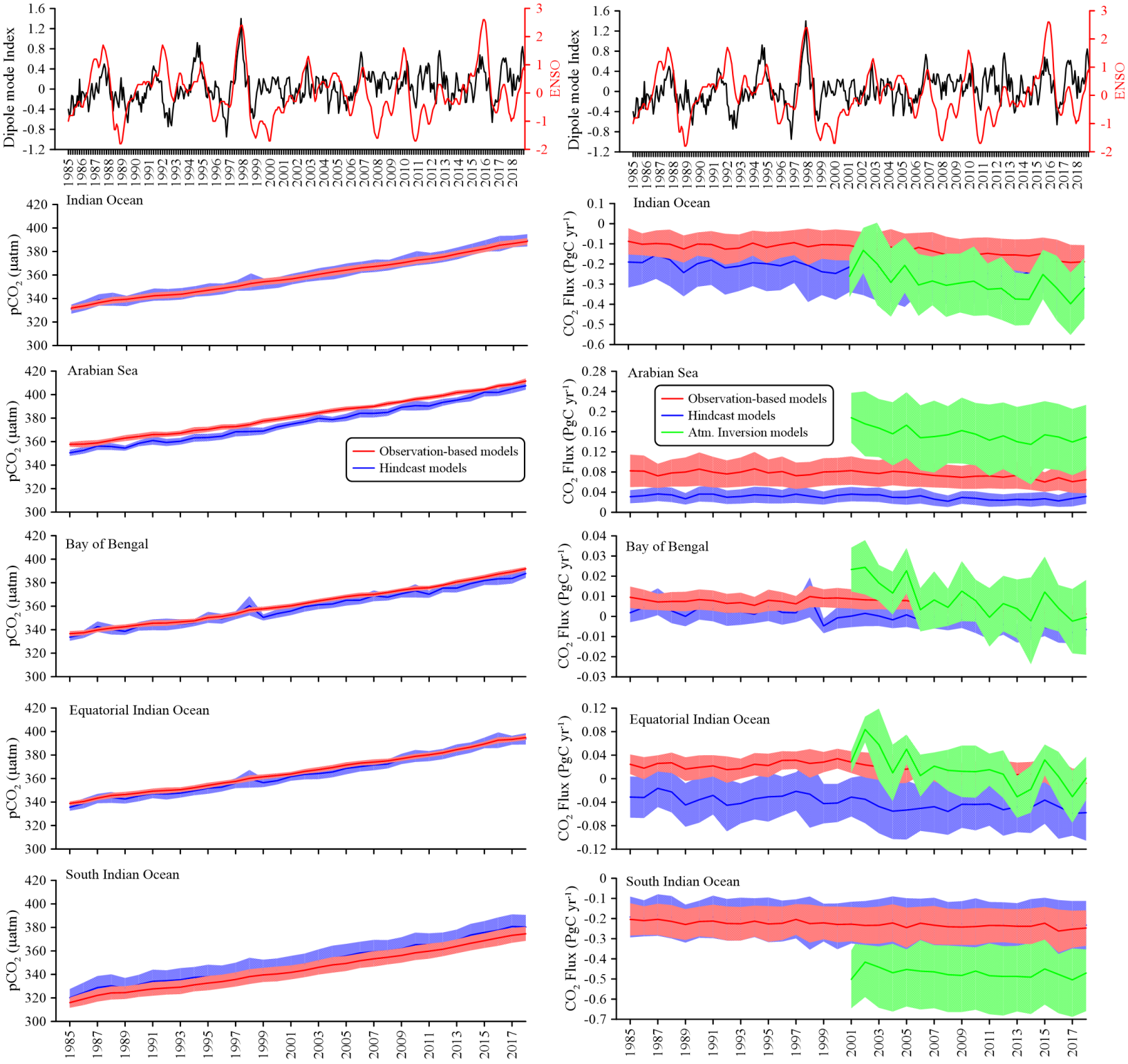
Dipole mode Index
ENSO
Indian Ocean
Arabian Sea
Bay of Bengal
Equatorial Indian Ocean
South Indian Ocean
pCO2 (µatm)
CO2 Flux (PgC yr-1)
Observation-based models
Hindcast models
Atm. Inversion models